Separation and Purification Technology 306 (2023) 122607

Contents lists available at ScienceDirect

Separation and Purification Technology

journal homepage: www.elsevier.com/locate/seppur

Microscopic production characteristics of tight oil in the nanopores of different CO_2-affected areas from molecular dynamics simulations

Yongcheng Luo [a,b,c,*], Xiangui Liu [b,c], Hanmin Xiao [b,c,*], Taiyi Zheng [d]

[a] College of Engineering Science, University of Chinese Academy of Sciences, Beijing 100049, China
[b] Institute of Porous Flow and Fluid Mechanics, University of Chinese Academy of Sciences, Langfang 065007, China
[c] Research Institute of Petroleum Exploration & Development, Beijing 100083, China
[d] Institute of Mechanics, Chinese Academy of Science, Beijing 100190, China

ARTICLE INFO

Keywords:
CO_2 EOR
Displacement-affected area
Diffusion-affected area
Nanopores
CO_2 solubility
Oil swelling
Oil potential energy

ABSTRACT

Understanding the mechanisms of CO_2 extraction or flooding are vital for enhancing oil recovery (EOR) in tight reservoirs. In this study, the CO_2 EOR mechanism in the displacement-affected area (DPAA) and diffusion-affected area (DFAA) of quartz nanopores were thoroughly investigated using molecular dynamics simulation techniques. First, the following two contents were mainly simulated, namely CO_2 flooding oil in the single/double nanopores of DPAA and CO_2 extraction oil in dead-end nanopores of the DFAA with and without the water film. Then, tight oil potential energy, threshold capillary pressure, CO_2 solubility, and oil swelling in nanopores were calculated to clarify the effects of CO_2 on oil transport. Moreover, different CO_2 injection/flowback rates and different water film thicknesses on dead-end nanopores on oil recovery were discussed. In the DPAA, the CO_2 solubility and the oil swelling factor gradually decreased with distance from the CO_2-oil interface (Y = 0 nm), where the higher the injection rate, the more easily the CO_2 dissolved in the oil. However, the injection rate of CO_2 was inversely proportional to oil recovery. In addition, it took longer for the displacement efficiency in the 6 nm pore of double pores to reach the same displacement efficiency as in the single 6 nm pore. In the DFAA, the effect of flowback rate on the displacement efficiency of oil was relatively low. However, the thickness of the water film was a key factor that affected the oil displacement efficiency in the DFAA.

1. Introduction

Tight oil as an unconventional energy source has gradually become an essential strategic replacement for traditional fossil fuels [1,2]. Statistics released by the Energy Information Administration (EIA) showed that in 2020, nearly 65% of total oil production in the U.S. was extracted from tight formations [3,4]. Tight oil reservoirs in China generally have the characteristics of strong heterogeneity, large variations and limited distribution, poor physical properties and fracture development, low permeability and porosity, and small pore throats. Therefore, the primary recovery factor has shown to be around 5–10% despite conducting massive hydrofracturing and long horizontal wells drilling operations [5-7], indicating a large amount of crude oil still remains in these tight formations. Thus, adopting effective methods to improve tight oil recovery has become an urgent issue to be solved. CO_2 has gained considerable attention in enhanced oil recovery (EOR) as a displacement medium that can be applied to reduce the crude oil viscosity and density, expand the crude oil volume, and reduce interfacial tension [8-10].

The methods of CO_2-EOR mainly include CO_2 injection [11-13], water alternating CO_2 (WAG) injection [14,15], and CO_2 huff and puff (HNP) [16-18]. Among these, the CO_2 HNP method has been mostly used for the production of single wells in tight reservoirs. Ding et al. [19] and Afari et al. [10] analyzed the effect of the HNP cycle number, injection rate, and the production bottom-hole pressure on EOR in their research. However, the interaction mechanism between CO_2 and crude oil was the key to CO_2-EOR. Liu et al. [20] conducted a CO_2 HNP experiment using an online nuclear magnetic resonance (NMR) instrument and found that the dissolved CO_2 drive controlled by molecular diffusion was the dominant mechanism in tight cores. Tang et al. [21] found through experimental research that the main CO_2 recovery mechanism was different in different CO_2-affected areas. In our previous study [22], the distribution of remaining oil in the different affected

* Corresponding author at: College of Engineering Science, University of Chinese Academy of Sciences, Beijing 100049, China (Y. Luo). Corresponding author at: Research Institute of Petroleum Exploration & Development, Beijing 100083, China (H. Xiao).
E-mail addresses: luoyongcheng18@mails.ucas.ac.cn (Y. Luo), xiaohm69@petrochina.com.cn (H. Xiao).

https://doi.org/10.1016/j.seppur.2022.122607
Received 7 October 2022; Received in revised form 30 October 2022; Accepted 6 November 2022
Available online 12 November 2022

areas during CO_2 NHP, which was obviously different between the displacement-affected area (DPAA) and the diffusion-affected area (DFAA), was further investigated.

Many experimental studies have been conducted to investigate the EOR potential of CO_2. However, in tight reservoirs with developed nanoscale pores, it is still a challenge to explore the oil production law of crude oil in nanopores in different affected areas with current experimental techniques. Therefore, molecular dynamics (MD) simulations have been used as a feasible and powerful tool to provide deeper insight into the liquid or gas properties at the nanoscale, which could help to understand dynamical, energetic, and structural properties at the molecular level [23-28]. Sedghi et al. [29] and Wang et al. [26] simulated pressure-driven oil flow mechanism in organic and inorganic nanopores. However, the effect of displacing CO_2 for displacing oil in nanopores was not considered. Liu et al. [30] used nonequilibrium molecular dynamics (NEMD) simulations to study the mechanisms of CO_2 displacement in nanopores under different CO_2 injection rates (2, 4, 6, 8, and 10 m/s). Fang et al. [31] used molecular dynamics simulations to study the CO_2 displacement process and found that the swelling effect of CO_2 was strong, while the propelling effect of CO_2 is weak. However, these researchers have studied the CO_2 displacement behavior in nanopores using one-component of oil such as octane and dodecane, without taking into account that oil was a very complex system. In addition, there was little research on the process of oil production in composite nanopores.

For the configuration variations of residual oil in dead-end nanopores, Fang et al. [32] investigated the mechanism of CO_2 hydrocarbon extraction with reservoir depressurization through MD simulations in dead-end nanopores. Moh et al. [33] investigated the soaking oil recovery mechanism of CO_2 HNP in a single, 4 nm-wide calcite dead-end pore using MD simulations. In natural oil reservoirs, oil will exist not only in nanopores, but the water phase will also be present. The existence of water phase changes the motion law of fluid in nanopores [34]. Moreover, the interaction between water and crude oil in nanopores is very different from that in bulk fluids [35]. Cui et al. [36] conducted microscopic visualization experiments and found that the thicker the water film, the longer the oil and carbon dioxide mixture required to reach the miscible phase. Luan et al. [37,38] used MD simulations as a research tool to explore how CO_2 displaced the residual oil in dead-end nanopores. In addition, the researchers simulated the rupture of the water film and discussed hydrogen bonds and the evolution of the collapsed pores.

Although scholars have conducted a considerable amount of research on the CO_2 displacement of oil in dead-end nanopores, the properties of oil cannot be truly reflected by using a single component of oil. The interaction between CO_2 and multi-oil components should not be ignored, which has a prominent response to CO_2-EOR methods in natural reservoirs. In addition, there is a lack of systematic research on the thickness of the water film.

This paper mainly studied the microcosmic recovery mechanism of multi-oil components in nanopores from the perspective of DPAA and the DFAA during the CO_2-EOR process. For DPAA, it was represented by the connected single/double quartz nanopore saturated with multi-component oil. Via the variation characteristics of the pressure threshold, CO_2 solubility, oil density, and potential energy, both the effects of pressure difference and injection rate on the oil recovery and the mechanism of CO_2 stripping oil molecules from quartz wall were simulated and analyzed. For DFAA, it was represented by the dead-end nanopore saturated with multi-component oil and water film. Through the variation characteristics of the same parameters, this paper discussed the recovery of different components, the effect of flowback rates on the displacement of oil, and the effect of water film thicknesses on the oil recovery.

2. Materials and research methods

2.1. Materials

The experimental core and oil both came from the Chang-7 oilfield. Regarding the basic physical properties of the core, the permeability was 0.0263 mD and the porosity was 10.787%. The core is 6.144 cm in length and 2.504 cm in diameter [22]. For light oil basic physical properties, the density of crude oil was 0.8230 g/cm3 at the ground condition and 0.7428 g/cm3 at the formation condition. Based on previous studies [39,40], in this work, we determined that C1–C4, C6, C10, C19, and C30 represented oil (please refer to the supplementary materials for specific information). Fig. 1 shows the molecules and conceptual oil used in the simulation.

2.2. Experimental setup and procedures

The flow chart of the CO_2 HNP experiment is shown in Fig. 2. The experimental setup was mainly composed of a core holder, displacement pumps (Q5000, Quizix, Tulsa, OK, USA), NMR equipment (MacroMR12, Niumag Analytical Company, China), and a microscope (AxioScope.A1 Carl Zeiss, Germany). The experimental procedures were described as follows. Experimental water was prepared with deuterium water with a salinity of 50 g/L, which can eliminate the nuclear magnetic signal during CO_2 HNP process. In this work, bound water was established in the core. For the CO_2 HNP process: (a) the injection time was 1 h, (b) the soaking was 5 h, and (c) the production time was 10 h, and (d) we repeated steps (a)–(c) for the CO_2 HNP process until five HNP rounds were completed. Record the hierarchical NMR (Spin echo-single point imaging (SE-SPI), T2 maximum was 10^4 ms, Echo Time (TE) was 0.3 ms, Waiting Time (TW) was 3000 ms.) T2 spectrum data of the cores during the test. For microscopic observations: (a) conduct anhydrous slicing, (b) use sandpaper to polish the non-observed surface so that the observed surface was parallel to the microscope platform, (c) obtain photographs under magnification [22].

2.3. DPAA and DFAA models

2.3.1. DPAA models

A simulation system consisting of a piston (helium nanoplates), displacement phase (CO_2), displaced oil phase (C1–C4, C6, C10, C19, and C30), and quartz pore was built to study the forced two-phase displacement in the nanopores, as shown in Fig. 3. The rock was modeled as quartz, which was the major constituent of sandstones [41]. Tight sandstone was initially saturated with water, and hydrogen atoms were added to the oxygen atoms on the quartz surface to simulate real geology [37,42,43]. For a single quartz nanopore (Fig. 3(a)), the width of the pore was 6 nm (The distance between atoms in the inner wall of a pore.), and the length of the pore was 16 nm (The outermost atomic distance in the pore length direction). The pore and the right side were filled with oil molecules, and the petroleum phase was pressurized by the He nanoplate on the right side. This was filled with CO_2 molecules on the left, and the CO_2 phase was pressurized by the He nanoplate on the left. For the double quartz nanopores (Fig. 3(b)), the width of the small (top) pore was 3 nm, and the width of the large (bottom) pore was 6 nm. The length of both pores was 19.6 nm. Oil molecules and CO_2 molecules were filled in e same way as the single pore, but with twice the number of molecules.

2.3.2. DFAA models

In the modeling process, a quartz block 9.5 × 6.1 × 12.6 nm3 in size with a 6.0 × 6.1 × 10.0 nm3 sized aperture or pore was built, as schematically shown in Fig. 4(a). The quartz surface of the DFAA model was treated the same as the DPAA model. Then a dead-end pore model including oils (represented by C1–C4, C6, C10, C19, and C30 molecules) was demonstrated, and a water film with a thickness of approximately

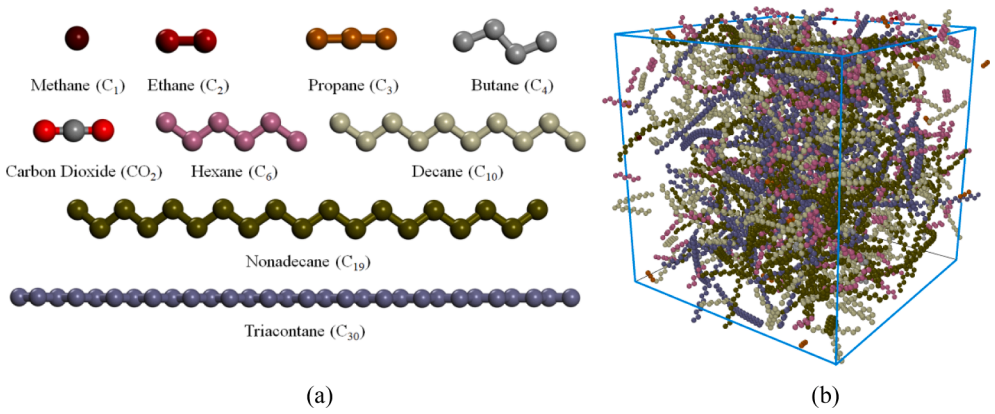

Fig. 1. Schematic diagram of oil molecular model: (a) oil components models, (b) light oil.

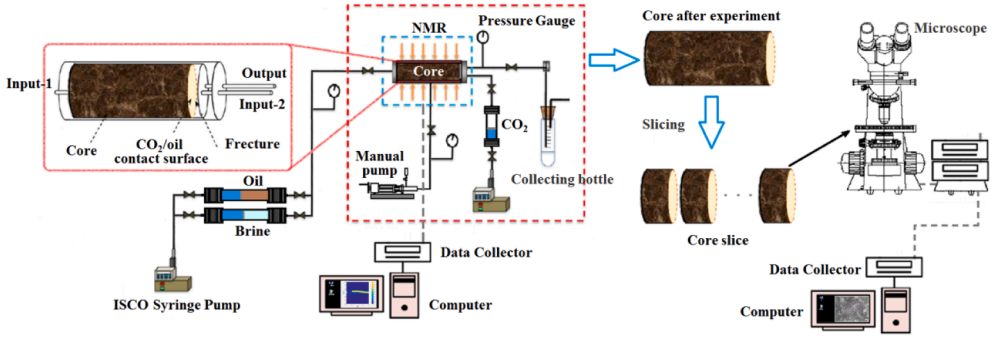

Fig. 2. The flow chart of CO_2 HNP experiment and microscopic observation [22].

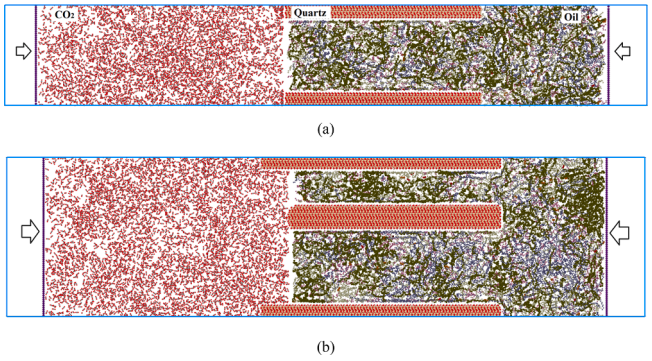

Fig. 3. Schematic diagram of the DPAA, (a) Simple pore, (b) Double pores.

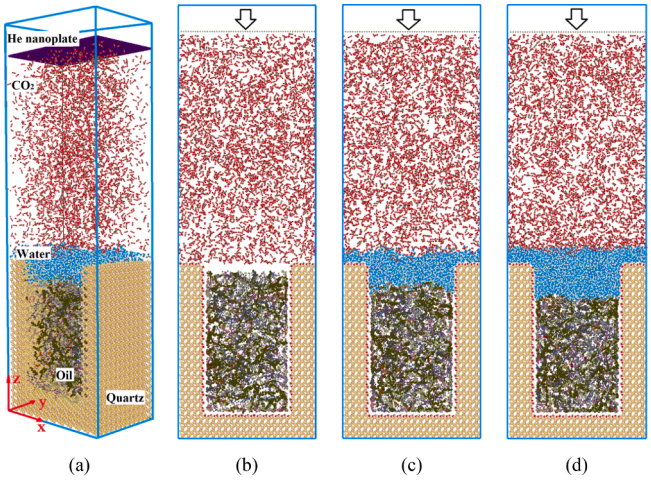

Fig. 4. Schematic diagram of the DFAA, (a) 3D schematic, (b) Without film, (c) 2.21 nm film, (d) 3.22 nm film.

0–3.22 nm on top of the pores was added (Fig. 5(b–d)). The existence of water film was a key factor for the exploitation of oil in dead pores [37,38]. CO_2 molecules were injected above the water film, and the injection pressure of CO_2 into the oil was provided by the downward pressure of the He sheet above.

2.4. Force field models

For the choice of forcefield, in this work, CO_2 was modeled using the EPM2 [44] forcefield, and the forcefield for CH4 was obtained from TraPPE-UA [45], while the NERD forcefield [46] was used for all other alkanes [39]. And the force field of water molecule selected the force field improved by Pekka et al. [47]. The CLAYFF force field [48] was adopted for the quartz substrates. The helium sheet, which had no gravity and no charge, applied P to the helium sheet to control the fluid system pressure. The non-bonded interactions between the atoms were described by the pairwise additive Lennard-Jones (LJ) 12-6 potentials and Coulombic interactions. Particle-particle-particle-mesh (PPPM) summation was applied to calculate the long-range corrections to the Coulombic interactions [27,49].

2.5. Molecular simulation details

MD simulations were performed using the large-scale atomic/molecular massively parallel simulator (LAMMPS) package [37,50], and the simulation configurations were visualized using Ovito Base software [35,39]. The boundary conditions were set to periodic boundary

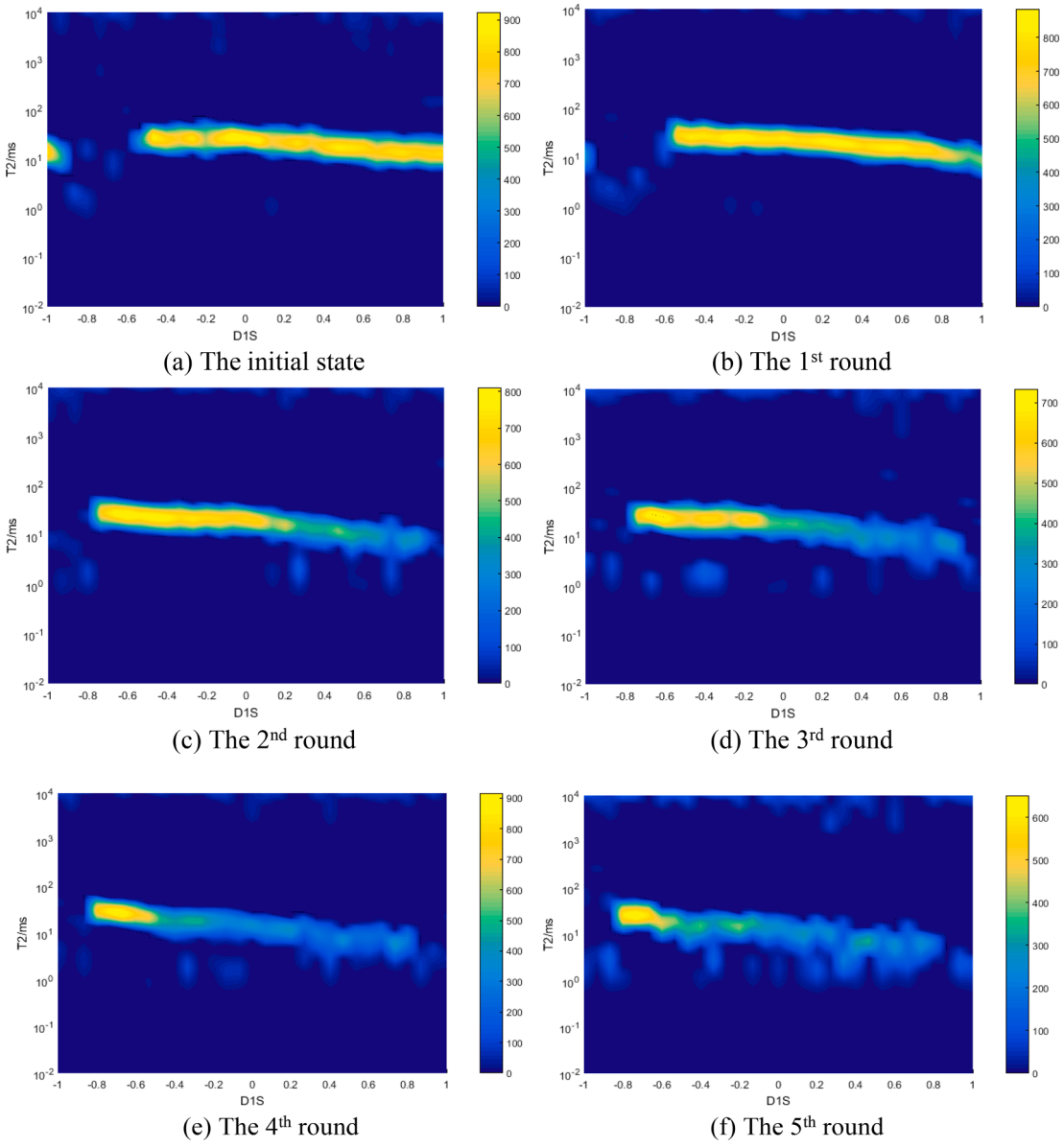

Fig. 5. T_2-SP (hierarchial T_2 spectrum) of the core #1 in 1st to 5th HNP rounds [22].

conditions, where the cutoff radius and time step were set to 12 Å and 1 fs, respectively. We performed energy minimization of the system by iteratively adjusting the atom coordinates, and the corresponding data were collected every 10 ps. The molecular model with constant volume and constant temperature (NVT ensemble) simulations proceeded in the CO_2–oil system, where the temperature and pressure were controlled using a Nose-Hoover thermostat [30,51] and Berendsen barostat, respectively [52,53].

2.5.1. DPAA models

For the simulation of the DPAA, the initial pressure of CO_2 and oil in the nano-pores was 10 MPa and the temperature was 345.15 K [22]. In this work, two flooding methods were used to displace oil: one was differential pressure flooding and the other was constant velocity flooding. The pressure differential displacement method was used to apply a fixed pressure of 10 MPa to the right helium sheet, and change the pressure applied to the left helium sheet, so that a pressure difference was generated between the left and right helium sheets. The resulting pressure differences were 0, 2, 4, 4.81, 6, 8, and 10 MPa, which were mainly used to analyze the pressure threshold of CO_2 and oil in nano pores. The constant-speed displacement method was relatively simple, where a fixed pressure of 10 MPa was applied to the helium sheet on the right, and a constant speed of 2, 4, 6, and 8 m/s was applied to the right of the left helium sheet to analyze the effect of injection rate on oil recovery law. The total simulation time of both methods was 7 ns.

2.5.2. DFAA models

For simulation of the DFAA, the initial pressure and temperature of the CO_2–oil or CO_2–oil–water in the dead-end nano-pore were 10 MPa and 345.15 K [22], respectively. There were two oil recovery methods in the DFAA: one was the equilibrium MD simulation oil recovery without flowback velocity, and the other was MD simulation oil recovery with flowback velocity (the flowback velocity values were 2, 4, and 6 m/s). The main purpose was to analyze the law of CO_2 recovery of oil in dead-end nanopores with or without flowback velocity. The method without flowback velocity was used to pressurize the system through the helium sheet first, and then fix the helium sheet, where the diffusion of CO_2 extracted the oil molecules in the dead-end pores. The oil recovery method with a flowback rate was used to pressurize the system through the helium sheet and fix the helium sheet after diffusion for 2 ns. A

constant velocity was applied to the helium sheet for constant oil extraction, where the total simulation time was 7 ns.

3. Experimental results and discussion

To explore the effect of CO_2 on the residual oil in the pores after each round of HNP, we performed T2 layer monitoring on the core after each round of HNP. The hierarchical T2 spectra of the core are shown in Fig. 5. Through the T2 map, we found that the contact front of CO_2 and oil gradually moved to the left with an increase in throughput rounds. Fig. 5(a-f) shows the intensity of the magnetic signal of the initial core and the intensity of the magnetic signal of the core after different HNP rounds. As can be seen from the figure, the oil in the core near the injection side was most easily recovered. And with the increase of HNP cycles, the oil near the end of the core was gradually recovered. In the process of CO_2 displacement of oil in the core, the oil content gradually decreases, so the H^+ particles in the core gradually decrease. However, the particles in CO_2 cannot be captured by the nuclear magnetic field, so the intensity of the nuclear magnetic signal gradually decreases with the increase of each round of HNP [54,55].

Fig. 6 shows the DPAA and DFAA in each CO_2 HNP round, which were primarily and severally determined based on the pressure difference and molecular diffusion [21]. Fig. 7 shows the microscopic images of the core sections at different locations after the CO_2 HNP experiment. Sequentially from the right (injection) end to the left end, the tinct of the slice core gradually darkened. This showed that the effect of CO_2 on residual oil displacement was obviously different in the DPAA and DFAA [22]. In the DPAA area, the oil recovery was high due to the pressure gradient and CO_2 displacement effect. In DFAA, CO_2 mainly expands the volume of oil through diffusion to produce oil, so the oil recovery rate was low. To explore the influence of CO_2 on the recovery of residual oil in the DPAA and the DFAA, in this work, we established a representative MD model representing the different affected areas, and further explored the microscopic oil recovery mechanism of CO_2 in the different affected areas.

4. Molecular simulation results and discussion

4.1. Displacement and sweeping law of DPAA in the nanopores

4.1.1. CO_2–oil potential energy and CO_2–oil–quartz interaction

Potential energy can reflect the stability of a substance, where the higher the potential energy, the more unstable the substance.

As shown in Fig. 8, CO_2 started to transfer into the oil after 2 ns. With increased simulation time, the potential energy of oil gradually increased, while the potential energy of CO_2 gradually decreased. The main reason for this phenomenon was because the dissolution of CO_2 in oil increased the distance between the oil molecules and reduced the activity space of the CO_2 molecules. From a macroscopic aspect, the above potential energy variation characteristics were manifested as dissolved CO_2 in the oil, reducing the oil viscosity and enhancing the oil fluidity.

Moreover, the dissolved amount of CO_2 in the oil was related to the position of the CO_2–oil interface, as also shown in Fig. 8(a), where the leftmost side in Fig. 8(a) represents the CO_2 injection end. Near the injection end, namely the CO_2–oil interface, the average atomic potential of oil was significantly higher than at other locations, indicating a higher dissolved amount of CO_2. As can be seen from Fig. 8(b), with the increase of time, CO_2 was gradually dissolved in the oil. Due to the strong adsorption capacity of CO_2 on the rock surface, the oil originally adsorbed on the rock surface would be stripped by CO_2, thus increasing the potential energy of oil. This was mainly because the adsorption capacity of CO_2 on the quartz surface was stronger than that of alkane molecules [56]. CO_2 and alkane molecules compete for adsorption on the quartz surface. Of course, the closer to the interface between CO_2 and oil, the greater the amount of CO_2 dissolved in the oil, and the more oil molecules cleaved from the quartz wall, the greater the average molecular potential energy of oil.

4.1.2. Threshold capillary pressure

The critical capillary pressure consists of the minimum pressure that a fluid must overcome to enter capillaries under hydrophilic conditions [57]. In this model, the threshold capillary pressure in the water-wetted quartz nano-pore was directly determined through measuring the pressure that could maintain the oil in equilibrium. The relevant details were as follows. (1) Different pressures were applied to the CO_2–oil system by moving the He sheets at both ends of the model under the condition of an initial pressure of 10 MPa and temperature of 345.15 K. (2) We then observed the centroid position of the oil to analyze the oil movement in the nano-pore. (3) When the centroid position remained unchanged, the CO_2–oil system was considered to be in equilibrium within the nano-pore. At this moment, the pressure difference of the He nanoplates was the threshold capillary pressure of the CO_2–oil system at the 6 nm pore.

Fig. 9 shows the centroid position of the oil when the pressure difference on the He nanoplates varied from 0 to 10 MPa. As shown in Fig. 9, when the pressure difference was 0 MPa, the oil centroid position moved in the direction of the positive Y axis, indicating that the water-wetted reservoir was favorable for CO_2 flooding. When the pressure difference was 4.81 MPa, the centroid position remains unchanged at about 14 nm in the Y direction. Hence, 4.81 MPa was the threshold capillary pressure of the CO_2–oil system at the 6 nm pore. When the pressure difference was greater than 4.81 MPa, the centroid position started to move in the direction of the negative Y-axis. This showed that the flowback pressure of oil was higher for the water-wet oil reservoirs during CO_2 HNP development.

4.1.3. CO_2 solubility and oil swelling in nano-pores

The CO_2 solubility and the oil swelling factor were key parameters to describe the strength of interactions between CO_2 and the oil. In the MD simulations, the CO_2 solubility and oil swelling factor were obtained by counting the molecular weight of the CO_2 dissolved in oil and calculating the ratio of the oil density before and after CO_2 diffusion, respectively. For better calculation results, the centroid position of the oil had to be stable. Hence, in this work, the model where the center of mass of oil was in equilibrium was applied to analyze the variation pattern of CO_2 solubility and the oil swelling factor with time and positions in the pores.

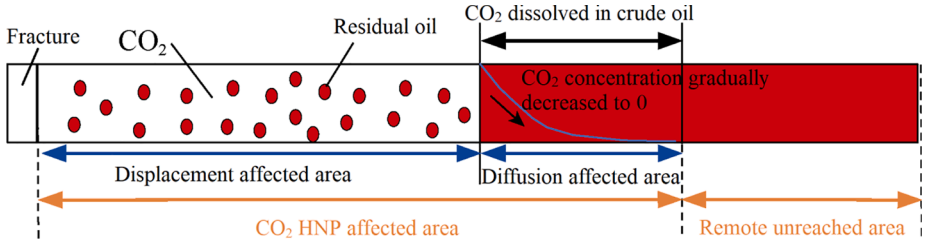

Fig. 6. Schematic of the DPAA and DFAA [21].

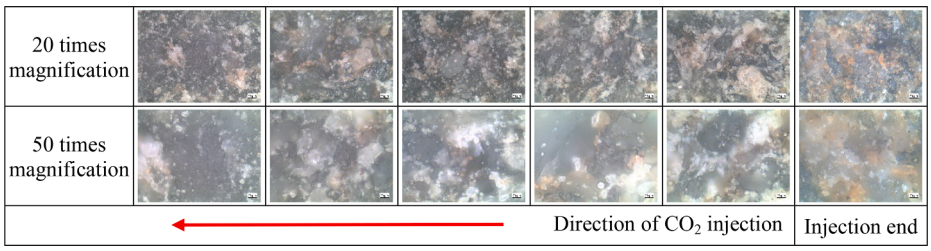

Fig. 7. Microscopic images of core sections at different locations after CO_2 HNP experiment [22].

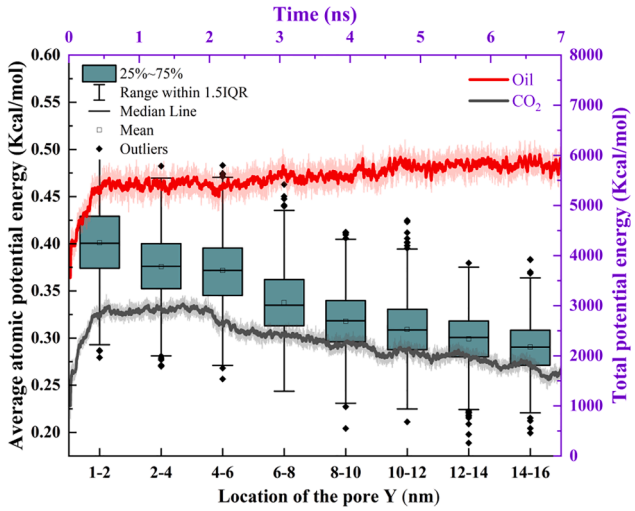

(a)

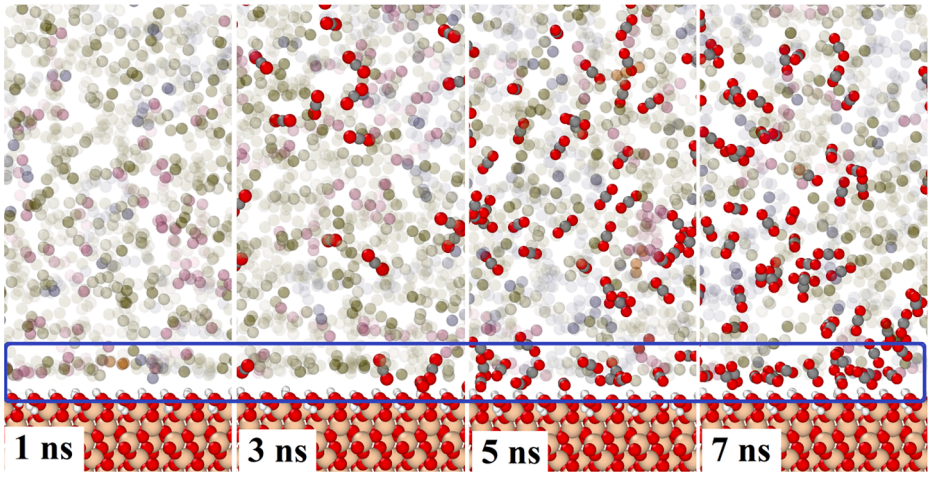

(b)

Fig. 8. Potential energy and distribution of CO_2 and oil in nanopores: (a)Average atomic potential energy of oil as a function of position and total potential energy as a function of time, (b) Distribution of CO_2 and oil molecules in pores at different times.

Fig. 10 shows the CO_2 solubility and oil swelling factors at different positions within the 6 nm pore at 4–7 ns. As shown in Fig. 10, as the simulation time advanced, the CO_2 solubility and oil swelling factor both increased to varying degrees. Moreover, the CO_2 solubility and oil swelling factor gradually decreased with distance from the CO_2–oil interface (Y = 0 nm). The consistency of the various behaviors of CO_2 solubility and the oil swelling factor indicated that the oil swelling factor was determined by CO_2 solubility.

4.1.4. Displacement of oil and CO_2

The oil density can intuitively analyze the distribution pattern of CO_2–oil system in nano-pores. Fig. 11 and Fig. 12 respectively show the oil density distributions along the Y and Z directions in the same nano-pore under various pressure differences of the He nanoplates. In Fig. 11, Y = 0 nm represents the initial interface position between CO_2 and the oil, and in Fig. 12, Z=±3 nm represents the nano-pore walls.

At a differential pressure of 2 MPa (<threshold capillary pressure), the oil density curve shifted along the y-axis with time and decreased obviously overall, as shown in Fig. 11(a). This meant that the CO_2–oil

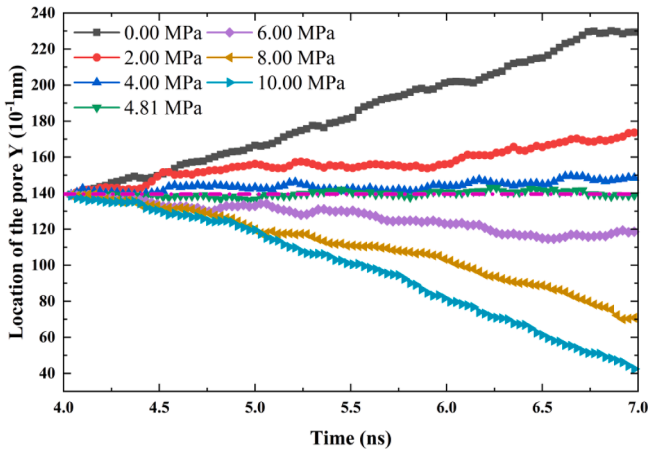

Fig. 9. The position of the center of mass of oil under different pressure differences.

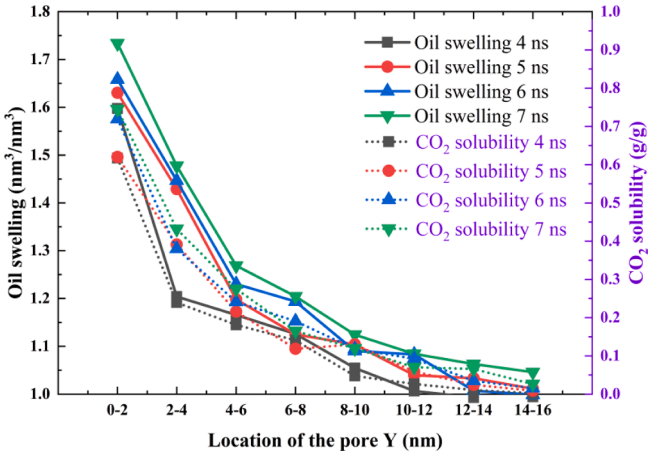

Fig. 10. CO_2 solubility and oil swelling factor at different positions within pore.

interface moved in the positive Y-axis direction during the CO_2 flooding process. As shown in Fig. 12(a), the oil density changed drastically in the area near the pore wall and the CO_2–oil interface. The amount of CO_2 adsorbed on the nano-pore wall was considerable, especially near the CO_2–oil interface, causing the oil adsorbed on the rock wall to be stripped off by the CO_2. Furthermore, the density curves of CO_2 and oil at 7 ns, Y = 4–6 nm could illustrate that CO_2 would preferentially strip the oil molecules adsorbed on the pore walls during the process of CO_2 flooding in the nanopores.

At a differential pressure of 4.81 MPa (=threshold capillary pressure), the oil density changed noticeably in the Y and Z directions around the oil-CO_2 interface region, as shown in Fig. 11(b) and Fig. 12(b). Furthermore, the oil density varied slightly under different time nodes. This group of simulations highlighted the effect of CO_2 diffusion on the oil density.

At a differential pressure of 8 MPa (=threshold capillary pressure), the oil density distributions in Fig. 11(b) and 12(b) were similar to those in Fig. 11(c) and 12(c), although the reasons for these distributions were different. Fig. 11(c) and 12(c) shows the oil flowback process in the pore under a constant driving pressure. The diffusion rate of CO_2 into oil was roughly equal to the oil flowback rate; thus, the oil density in the pore remained basically constant.

4.1.5. *Effect of injection rate on the transport of oil*

Since the CO_2 injection rate is crucial for CO_2 flooding, the effect of CO_2 injection rate on the oil displacement efficiency in the nano-pores should be deeply explored. In this work, the pressure of the CO_2–oil system was maintained at about 10 MPa. Constant velocities of 2 m/s, 4 m/s, 6 m/s, and 8 m/s in the positive direction of Y were applied to the He nanoplate at the CO_2 end, with the equivalent CO_2 injection velocity [30].

Fig. 13 shows the density distributions of CO_2 and oil in the Z direction at different injection rates at different times. When the velocity was 2 m/s, the interface position at 7 ns was about 8–10 nm. At the CO_2–oil interface, the oil on the nano-pore wall was peeled off. When the injection speed reached 6 m/s, the oil in the pore was basically displaced at 7 ns, but some oil molecules still remained. At a CO_2 injection speed of 8 m/s, the CO_2–oil interface reached 14–16 nm at a time of 6 ns. At 7 ns, in the range of 0–6 nm near the injection end in the pore, the oil

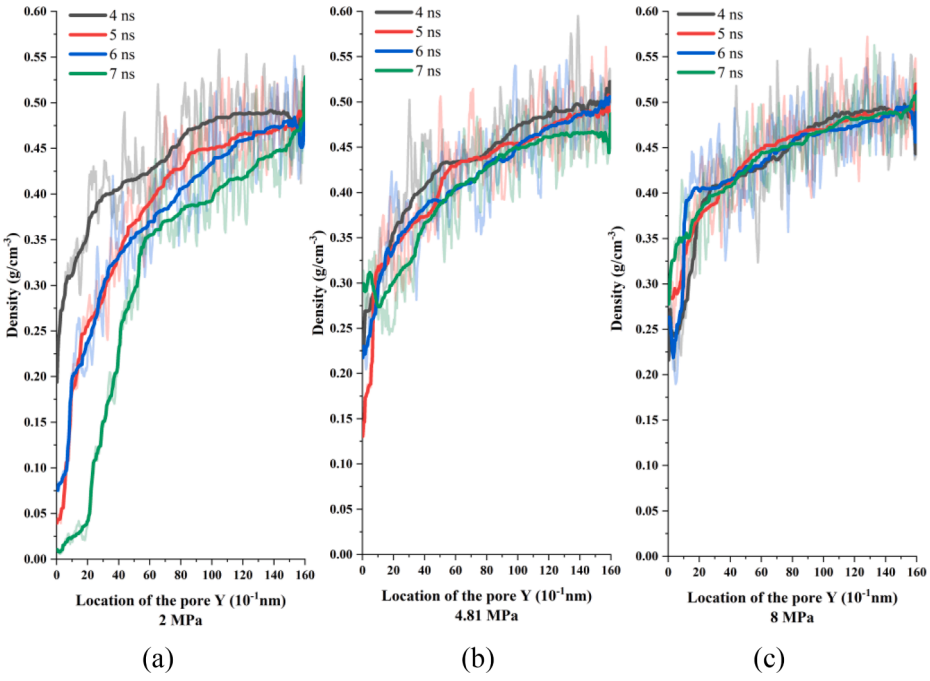

Fig. 11. Density distribution of oil under different pressure differences: (a) 2 MPa, (b) 4.81 MPa, (c) 8 MPa.

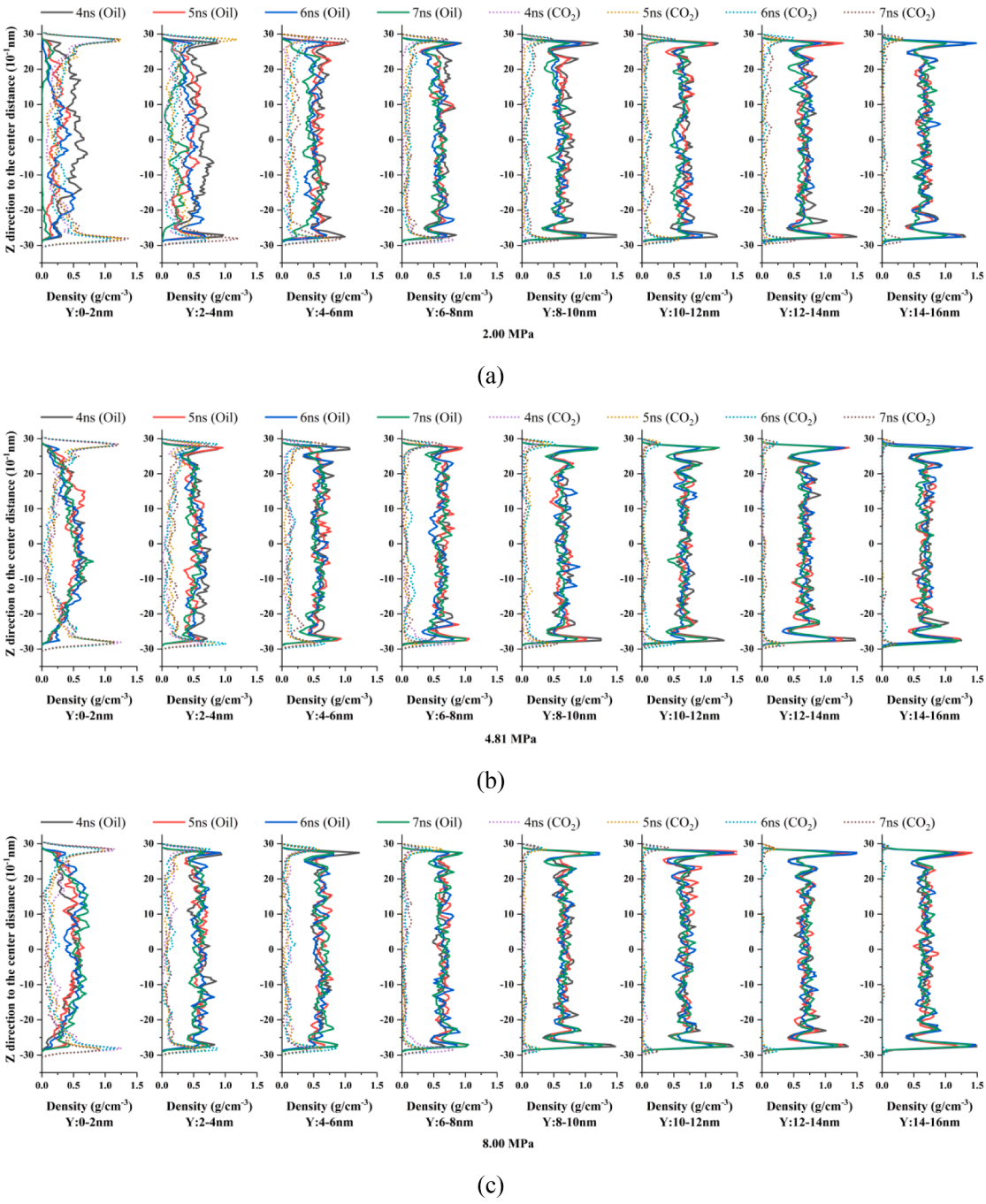

Fig. 12. Density distribution of oil at different positions under different pressure differences: (a) 2 MPa, (b) 4.81 MPa, (c) 8 MPa.

displacement was relatively clean. In the range of 6–14 nm, there were still some residual oil molecules.

CO_2 displacement within the nano-pore was linear (Fig. 14A). At different injection speeds, the position of the center of mass of the oil moved linearly in the Y direction with an increase in simulation time. Fig. 14B shows that the number of CO_2 atoms displacing the oil from the pore also increased linearly with time. The CO_2 displacement efficiency of the oil in the nano-pore was calculated according to the ratio of the atomic number of the displaced oil to the total atomic number of the oil. When the displacement speeds were 6 m/s and 8 m/s, the oil displacement in the pore basically ended at 7 ns, and the final displacement efficiency was about 90%. About 10% of the oil molecules remained in the nano-pore. When advancing the same distance, the injection speed, the lower the efficiency of CO_2 displacement of the oil. Taking a propulsion distance of 2 nm as an example, the displacement efficiency of 2 m/s was 52.01%, while the displacement efficiency of 8 m/s was only 27.65%. This indicated that the displacement rate of CO_2 should not be too high when using CO_2 for oil displacement. Fig. 14c shows the different components' displacement efficiency at a CO_2 injection rate of 8 m/s. As can be seen from the figure, except for the displacement efficiency of C1-C4, the displacement efficiency of other components gradually decreased with the increase of the carbon chain. The main reason was that some of the light molecules of C1-C4 move into the CO_2 gas phase, resulting in the reduction of its recovery rate. At the same time, the longer the molecular chain in the nanopore, the harder it was to drive.

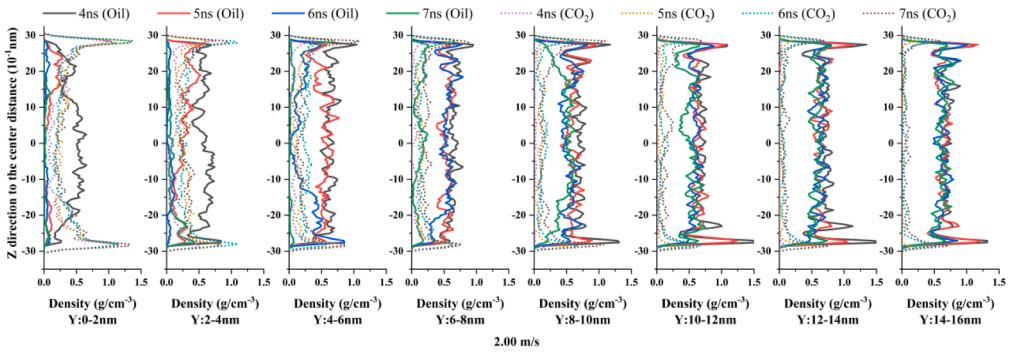

(a)

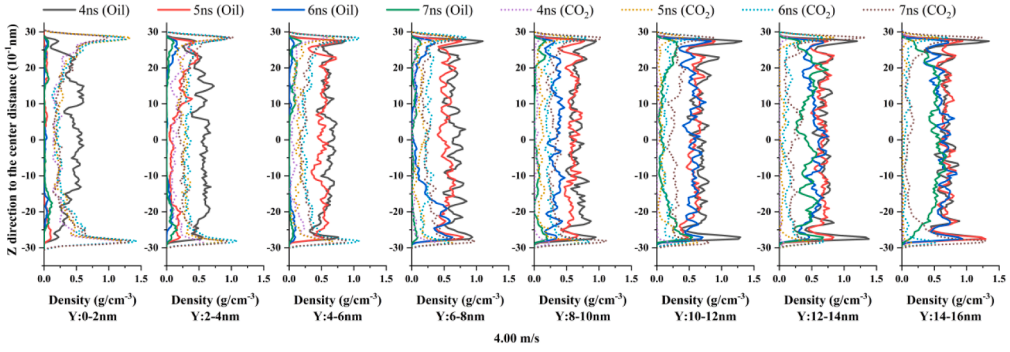

(b)

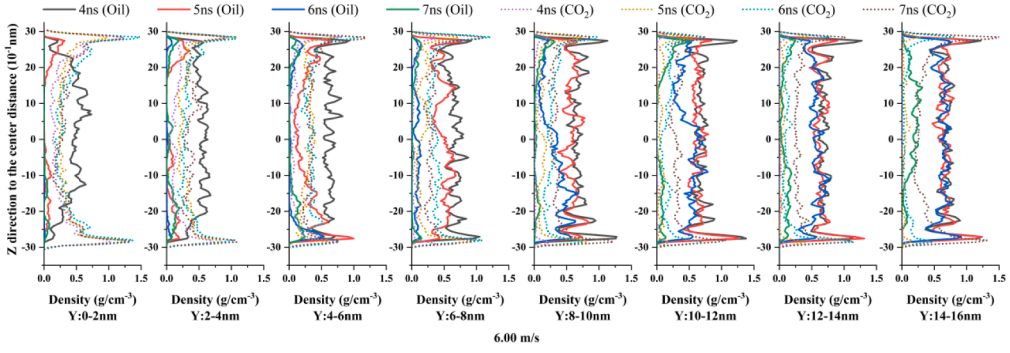

(c)

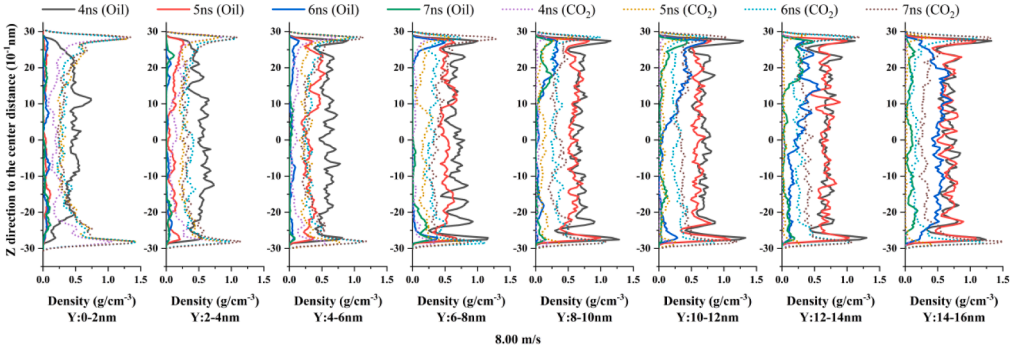

(d)

Fig. 13. Density distribution of oil under different CO_2 injection rates: (a) 2 m/s, (b) 4 m/s, (c) 6 m/s, (d) 8 m/s.

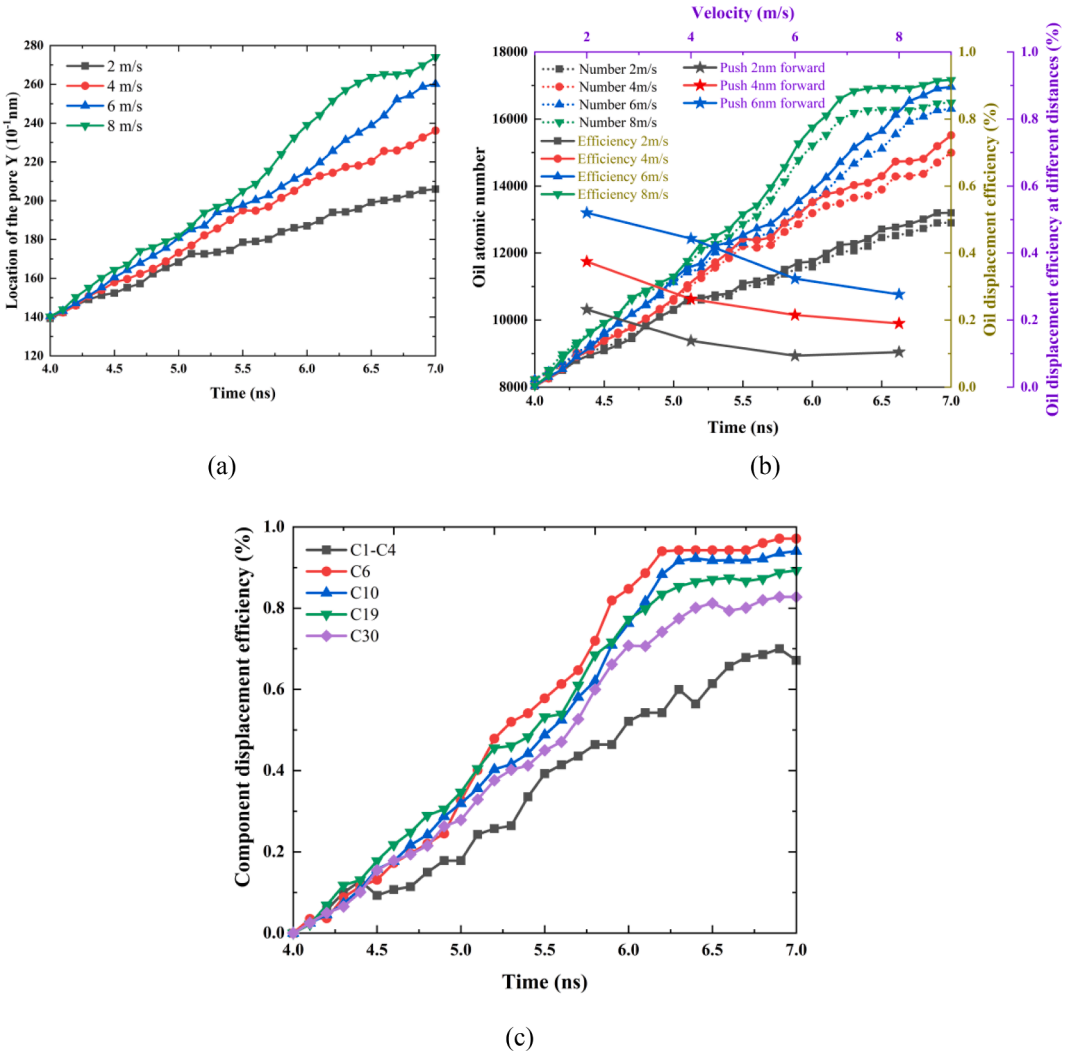

Fig. 14. Displacement efficiency of oil under different CO_2 injection rates: (a) Movement of the position of the center of mass of oil, (b) The number of atoms displaced by oil, the displacement efficiency of oil over time and the displacement efficiency of oil advancing the same distance at different injection rates, (c) The component displacement efficiency at the injection rate of 8 m/s.

4.1.6. *Interfacial behavior of CO_2 and oil at different injection rates*

As shown in Fig. 15, we explored the CO_2 and oil interfacial behaviors at different injection rates. When the injection rate of CO_2 was 2 m/s, the tangent slope of the oil density distribution at the interface was larger than the density distribution of oil in the nanopores. As the simulation time increased, the CO_2–oil interface moved forward overall. With an increase in the injection rate, the slope of oil density at the interface gradually decreased, indicating that the interface between CO_2 and oil gradually became blurred with an increase in the injection rate. The higher the velocity, the smoother the density distribution of oil at the interface, and the wider the interfacial band of CO_2–oil. This showed that when the injection rate was higher, CO_2 was more easily dissolved in the oil.

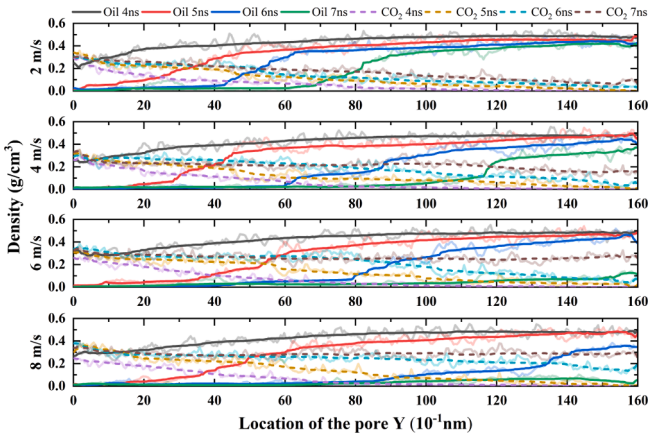

Fig. 15. Variation of the interface between CO_2 and oil with time under different CO_2 injection rates.

Comparing the density distribution of CO_2 at different injection velocities at Y = 14–16 nm, the density of CO_2 increased slowly with an increase in simulation time under injection velocities of 2 m/s and 4 m/s. However, at injection speeds of 6 m/s and 8 m/s, the density of CO_2 increased slowly when the CO_2 injection interface did not reach Y = 14–16 nm. When the CO_2 injection interface reached Y = 14–16 nm, the density of CO_2 increased rapidly. The main reason was that the CO_2 density in oil was mainly caused by the diffusion of CO_2 molecules when the CO_2–oil interface was not reached. When the CO_2–oil injection interface reached Y = 14–16 nm, the oil in the pore was displaced by CO_2 and the pore was filled with CO_2 gas.

4.1.7. *Displacement of oil and CO_2 in dual pores*

The combined pore structure is considered a true reflection of the

complex pore structure of tight reservoirs. To explore the law of CO_2 flooding oil in combined pore structure, a combination model with small pores of 3 nm and large pores of 6 nm was established in this work. Fig. 16 shows the CO_2 and oil density distributions in the Z direction when the CO_2 injection velocities were 4 m/s and 8 m/s. As the simulation time increased, the density distribution of oil with large pores changed more significantly than the small pores. Compared to the single pores, the displacement efficiency of the double pores was relatively slow. When the injection speed was 4 m/s (Fig. 16(a)), and the simulation time reached 7 ns, the oil in the single pore was displaced to the end of the pore. For double pores, the displacement front of CO_2–oil in the macropores was at Y = 6–8 nm (for comparison with single pores, Y = 16 nm in the double pores was considered to be the end of double pores). When the injection speed was 8 m/s (Fig. 16(b)), when the simulation time reached 7 ns, the CO_2-flooded oil in the large pores in the double pores was also displaced to the end. However, comparing the distribution of oil density in single pores, we found that more oil molecules remained on the walls of the large pores in the double pores.

As shown in Fig. 17, we could better determine that under the same injection rate, the displacement rate of the double pores became slower. Oil in the small pores was relatively difficult to drive. At an injection speed of 4 m/s (Fig. 17(a)), the CO_2–oil interface in the small pores only reached about Y = 2–4 nm at a time of 7 ns. Under an injection speed of 8 m/s (Fig. 16(b)), the oil in the large pores was displaced at 7 ns, while the CO_2–oil in the small pores only reached about Y = 6–8 nm. Therefore, compared with single pore of the same scale, the combined multi-

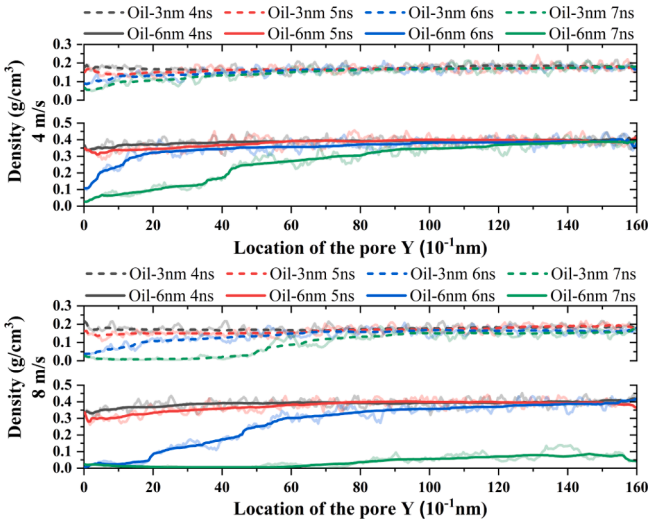

Fig. 17. Variation of the interface between CO_2 and oil with time under different CO_2 injection rates.

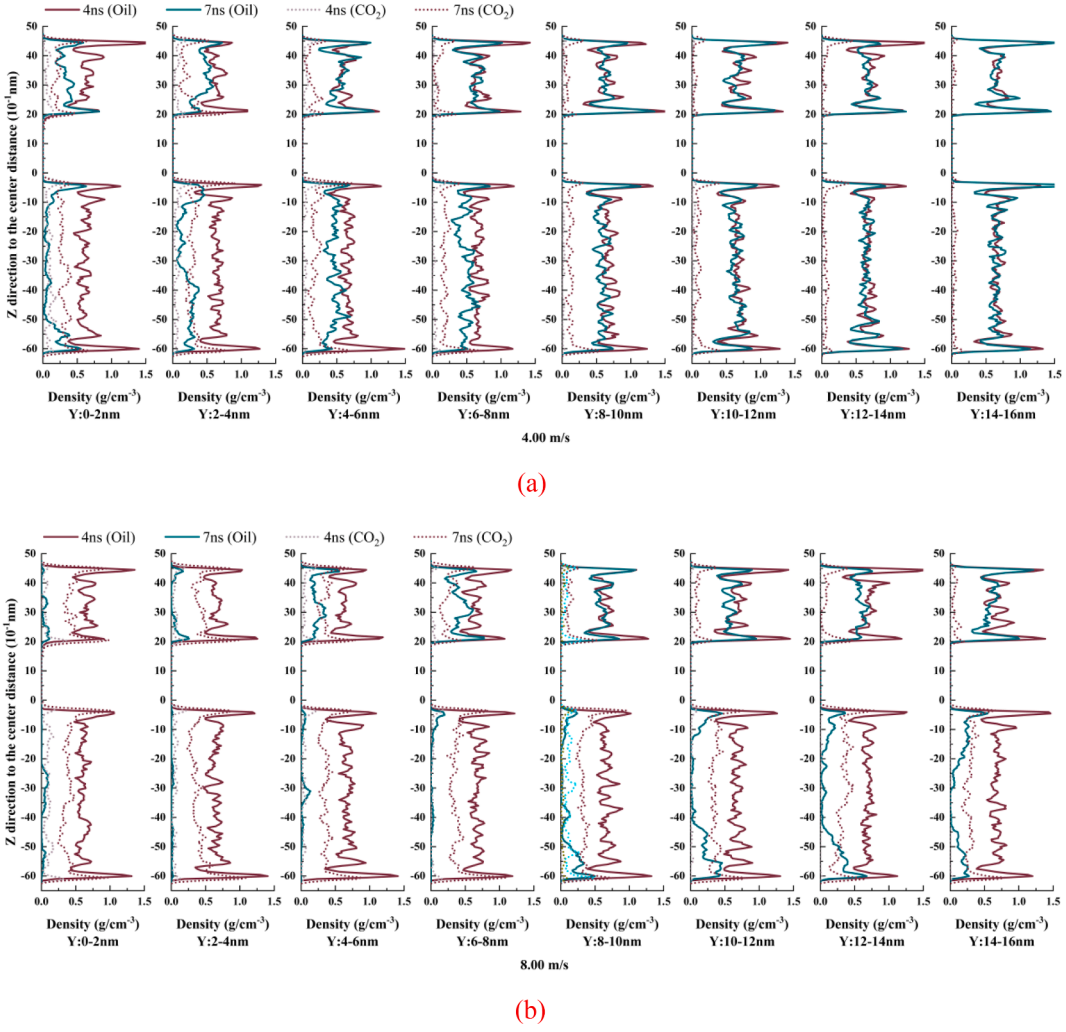

Fig. 16. Density distribution of CO_2 and oil under different CO_2 injection rates: (a) 4 m/s, (b) 8 m/s.

pore model with small pores would slow down the displacement efficiency of oil, requiring longer displacement time.

4.1.8. Influence of dual pores and single pores on the oil displacement efficiency

We compared the CO_2 displacement efficiency of oil under the same injection conditions between the single-pore and dual-pore models. As shown in Fig. 18, when the CO_2 injection rate was 4 m/s, the displacement efficiency at 7 ns in a 6 nm single pore was 75.14%, while the displacement efficiency of 6 nm pores in the model with small pores was 41.38%. The displacement efficiency at 7 ns in the 3 nm pores in the double pores was 22.80%, and the comprehensive displacement efficiency in the double pores was 36.26%. This was mainly caused by the low displacement efficiency in the small pores of double pores. When the CO_2 injection rate was 8 m/s, the displacement efficiency of the 6 nm pores in the double pores was the same as the 6 nm single pores at 7 ns (about 90%). However, under the same conditions, the displacement efficiency of 6 nm in single pore was shorter than that in double pore when the displacement efficiency of 6 nm reaches 90%. At 7 ns, the displacement efficiency of 3 nm in the double pores was 52.84%, and the comprehensive displacement efficiency was 80.17%. The addition of small pores reduces the displacement efficiency of oil. Furthermore, it took longer for the displacement efficiency in the 6 nm pore of double pores to reach the same displacement efficiency as in the single 6 nm pore.

4.2. Oil recovery law of the DFAA in the nanopores

4.2.1. Potential energy of oil in different locations

In dead-end nanopores, the potential energy of oil will be related to the depth of oil in the dead-end pores. Under 345.15 K and 10.0 MPa, the affected mode of CO_2 in the closed pores with a width of 6 nm was mainly the CO_2 molecular diffusion. To explore the oil potential energy distribution after CO_2 diffusion in dead-end nanopores, in this work, the equilibrium molecular dynamics (EMD) method was used to simulate the average atomic potential energy of oil at different positions in the closed pores when the fixed Up-He nanoplate CO_2 diffused to 7 ns. The non-equilibrium molecular dynamics (NEMD) method was used to apply different velocities in the positive Z direction to the Up-He nanoplate to the average atomic potential energy of oil at different positions in the dead-end pores when the speed reached 7 ns (Fig. 19).

The depth of the dead-end nanopore was 10 nm, and the average potential energy of the atoms in a layer was calculated by using 2 nm as a layer. The Up-He nanoplates were immobilized to ensure that the effect of CO_2 was only molecular diffusion. Taking the pink layer in the figure as the first layer, the average potential energy of the atoms in the dead-end pores increased gradually with an increase in the number of layers, and the first layer of atoms had the lowest average potential energy. This showed that the oil molecules were relatively stable at the bottom of the dead-end pores. The average atomic potential energy of oil increased gradually with an increase in the number of layers, and the atomic potential energy of oil was the largest at the interface between CO_2 and the oil (the fifth layer). This showed that the oil molecules produced at the interface were the most unstable and the easiest to produce dead-end pores. The average potential energy of the first layer of oil atoms was 0.4236 Kcal/mol at 7 ns, and the average potential energy of the 5th layer of oil atoms was 0.5875 Kcal/mol at 7 ns. When the Up-He nanoplate moved in the positive direction of Z at an average speed of 4 m/s, the average atomic potential energy of oil in the dead-end pores showed the same law. However, when the Up-He nanoplate moved toward the positive direction of Z, the pressure in the pores gradually decreased, and the distance between the molecules increased. Therefore, the average atomic potential energy of oil within the same layer was larger than oil when the Up-He nanoplates are immobilized.

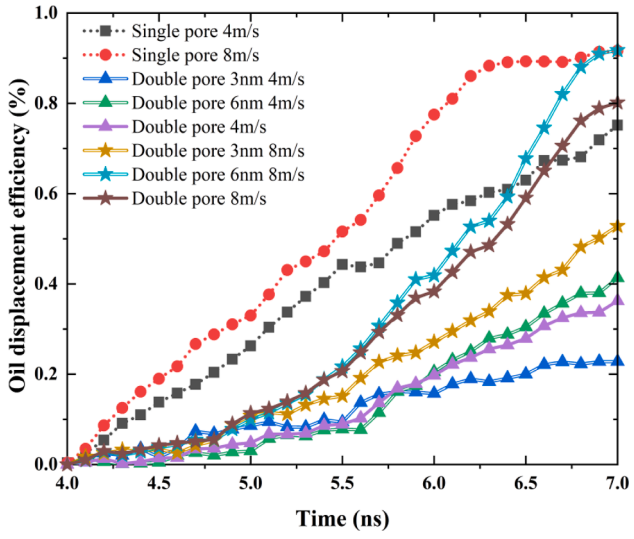

Fig. 18. Displacement efficiency of oil in different pores.

4.2.2. Density distribution characteristics of the oil and CO_2 in the dead-end pores

In the process of CO_2 HNP, the flowback rate of CO_2 is considered one of the key factors that will affect the efficiency of CO_2 HNP. To explore the effect of CO_2 flowback rate on the production law of oil in dead-end pores, we compared the density distributions of CO_2 and oil in the X and Z directions without and with flowback velocities in Fig. 20 and Fig. 21.

As shown in Fig. 20, the larger the flowback velocity, the less noticeably the oil density in the dead-end pores changed with the simulation time. When the flowback velocity was 6 m/s, the density distribution of the oil in the dead-end pores barely changed with an increase in simulation time. With no flowback velocity, the dissolved CO_2 in the oil in the dead-end pores gradually increased with simulation time. The difference was that with an increase in the flowback rate, the amount of CO_2 that dissolved into the oil gradually decreased.

Fig. 21 reflects the density distribution of CO_2 and oil in the X direction at different positions on the Z axis. Due to oil volume expansion caused by CO_2, when there was no CO_2 flowback velocity, in the region of Z = 2.6–4.6 nm, the oil density at the bottom of the dead-end pores gradually decreased with an increase in simulation time. In the region of Z = 2.6–4.6 nm, the oil density at the outlet of the dead-end pores gradually increased with simulation time. With flowback velocity, the oil density distribution in the X direction at different positions of the dead-end pores presented the same law; however, this law became less obvious with an increase in the flowback velocity.

4.2.3. Different oil component recovery factors by CO_2 molecular diffusion

In the DFAA, the diffusion of CO_2 was dominant in oil recovery. The dead-end pore model was used as the DFAA to explore the oil recovery mechanism of CO_2 diffusion. Fig. 22 shows the oil recovery of different components in oil due to CO_2 diffusion when CO_2 had no flowback rate. As shown in the figure, the oil recovery of C1–C4, C6, C10 were respectively 65.46%, 1.98%, and 18.41%, while C19 and C30 were meager at 1.79% and 0.00%. Therefore, when CO_2 was used to recover oil in the dead-end pores, the light components in oil were most easily recovered, making it difficult to recover the heavy components that remained in the dead-end pores. This also confirmed the reason why the oil recovery continued to decrease with an increase in CO_2 throughput rounds in the experiment. The comprehensive recovery rate of oil in the dead-end pores was 11.05%, which was very low compared to the flooding-affected area. The main reason for this was that the diffusion of CO_2 caused the oil system to undergo component differentiation. In conventional oil recovery, light components in oil were easier to recover, while components with higher carbon chains were more difficult to recover, such as heavy oil. Therefore, restraining or reducing the

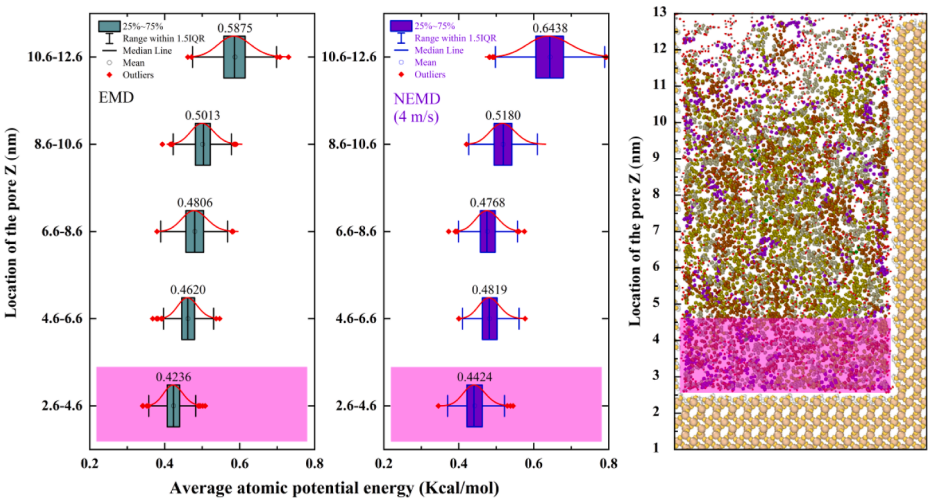

Fig. 19. EMD simulation and NEMD simulation of oil average atomic potential in dead-end nanopore as a function of position.

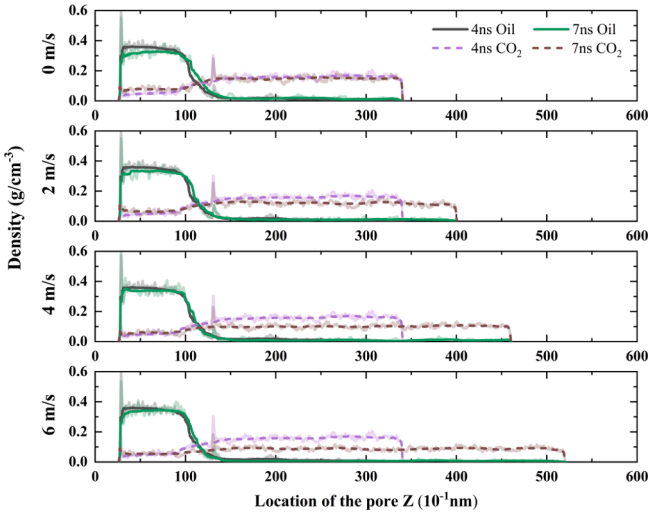

Fig. 20. Density distribution of CO_2 and oil at different CO_2 flowback rates.

component differentiation effect of CO_2 on oil was the key to improving oil recovery in the DFAA.

4.2.4. *Oil and oil component recovery factors under different flowback rates*

In this work, we established the production situation of oil with no flowback velocity and flowback velocity from 2 to 6 m/s in dead-end pores. Fig. 23 shows the oil recovery in dead-end pores at different flowback rates. Under different flowback rates, the oil recovery of the first increased rapidly and then tended to stabilize with increasing simulation time. The oil recovery without flowback velocity was 11.06%, while the oil recovery (11.07%) when the flowback velocity was 2 m/s was not much different from without flowback velocity. When the flowback velocity was 4 m/s and 6 m/s, the oil recovery were 10.77% and 10.18%, respectively. When the flowback rate increased gradually, the oil recovery in the dead-end pores was relatively low. The main reason for this was that the CO_2 gas dissolved in the pores and the light components in the oil easily precipitated with a faster flowback rate, resulting in a decrease in the overall recovery factor.

This could also be derived from the recovery of the different components at different flowback rates (Fig. 24). As shown in Fig. 24, the greater the flowback rate, the greater the recovery of C1–C4 in the oil.

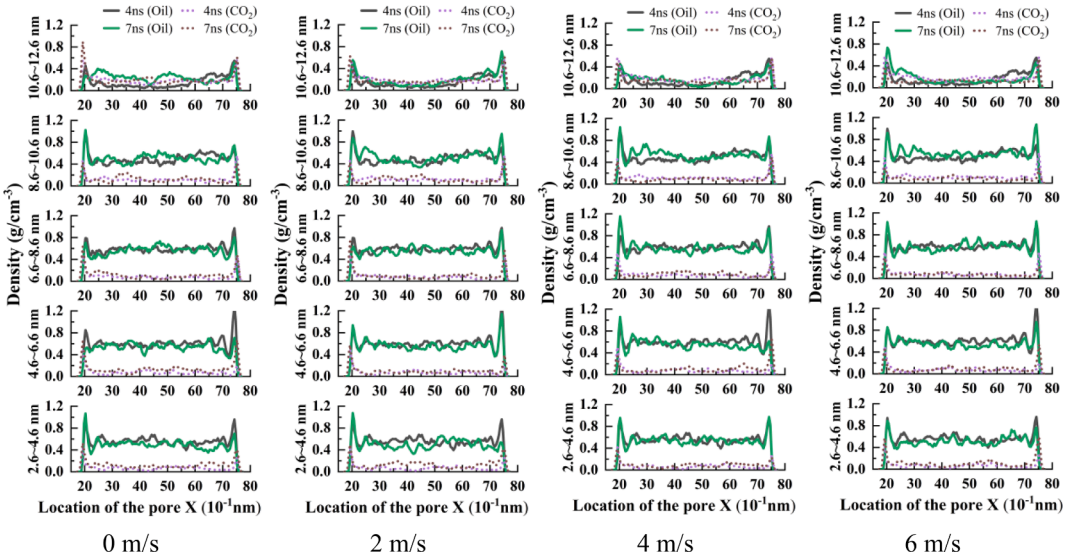

Fig. 21. Density distribution of CO_2 and oil at different locations at different CO_2 flowback rates.

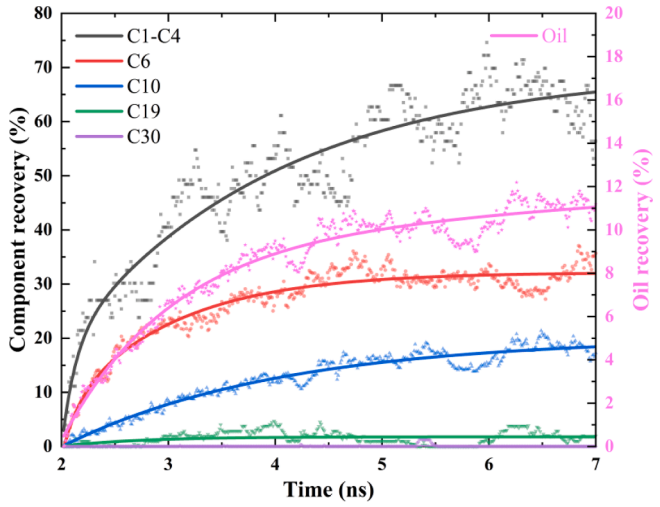

Fig. 22. Recovery factor of different components in oil without CO_2 flowback rate.

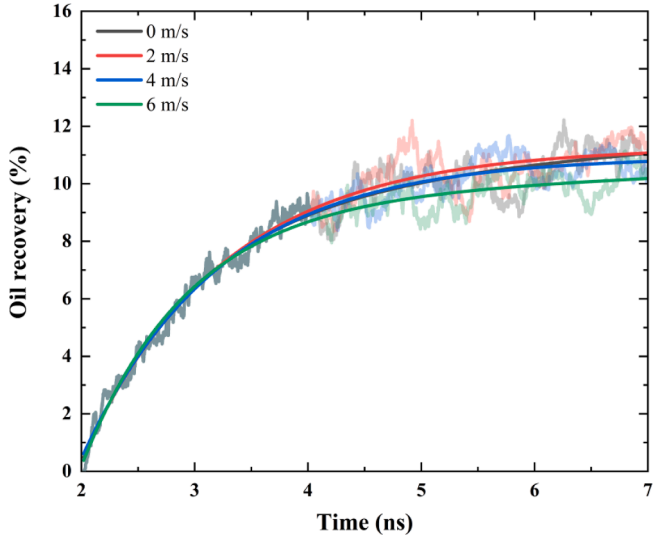

Fig. 23. Oil recovery under different CO_2 flowback rates.

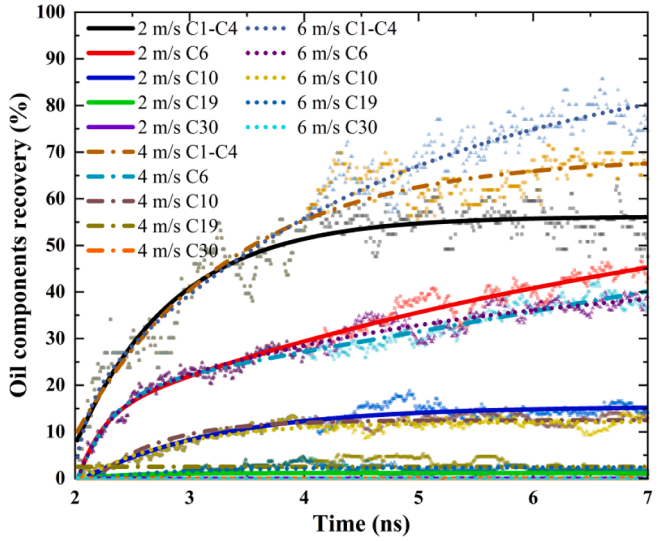

Fig. 24. Recovery factor of oil components under different CO_2 flowback rates.

When the flowback velocities were 2 m/s, 4 m/s, and 6 m/s, the recovery degrees of C1–C4 were 80.24%, 67.53%, and 56.06%, respectively. We found that the greater the flowback speed, the greater the recovery of C1–C4 with the mining time. This showed that the greater the flowback, the greater the depressurization rate in the system, and the easier precipitation of C1–C4 components. However, the higher the flowback rate, the lower the recovery of the other components in the oil. Taking the recovery of C10 as an example, when the flowback speeds were 2 m/s, 4 m/s, and 6 m/s, the recovery degrees were 15.18%, 12.51%, and 12.13%, respectively. We observed that the flowback rate of CO_2 was high during oil recovery, which caused the heavy components in the oil to remain in the dead-end pores and be more difficult to recover.

4.2.5. Density distribution characteristics of the oil and CO_2 under different water films

In a real geological reservoir, the state of the fluid in the formation will be very complex, and generally a water phase will be present [58,59]. In the DPAA, the presence of aqueous phase will also be displaced out of the pores by CO_2. In the DFAA, the existence of water film was the key to hinder the recovery of oil in dead-end pores. To consider the influence of water flooding or the existence of water film on CO_2 production, in this work, water films with different thicknesses were established to compare the effects of water films of different thicknesses on oil production. Fig. 25 shows that when the water film thickness was 2.21 nm, the water film that closed the pores was broken during CO_2 injection process. Because the walls of the pores were water-wetted, the ruptured water film would gradually enter the pores due to the imbibition of water, and the oil molecules that peeled off originally were adsorbed on the surfaces of the pores. Fig. 26 shows that when the water film thickness was 3.22 nm, the water film enclosed on the pores did not rupture during CO_2 injection process. The oil molecules and the water film in the dead-end pores reached a dynamic equilibrium, and the oil in the dead-end pores could not be recovered.

Fig. 27 shows the CO_2 and oil density distributions of oil on the Z-axis with water film of 0, 2.21 nm, and 2.21 nm. As shown in the figure, when the anhydrous membrane was present, the oil density in the pores decreased gradually with increasing simulation time. This was mainly due to the dominance of diffusion and the dissolution of CO_2 into the oil. When the water film thickness was 2.21 nm, the oil density in the pores decreased rapidly after breakthrough of the water film. The main reason was that the oil in the pores had a flow channel after water film breakthrough. Because the pore walls were wetted by water, the water molecules gradually moved into the dead-end pores, so that more oil molecules were displaced by the imbibition of water. When the water film thickness was 3.22 nm, the dissolved amount of CO_2 in oil was relatively small due to the blocking of the water phase. In addition, there was no breakthrough in the water film, and the oil in the dead-end pores was difficult to recover. The water–oil–gas reached a dynamic equilibrium in the dead-end pores; therefore, it was necessary to consider whether CO_2 could effectively make contact with the oil when using CO_2 for oil flooding in reservoirs with high water content.

4.2.6. Influence of water film on recovery rate

To further analyze the influence of water film on the oil recovery rate of CO_2 in closed pores, in this work, we used dead-end pores as the benchmark, and the oil molecules produced from the pores were considered to be recoverable. Therefore, the ratio of the oil molecules in the dead-end pores to the total number of oil molecules was the oil recovery in the dead-end pores. Fig. 28 shows the oil recovery in the pores in the presence of water membranes with different thicknesses. The oil recovery with 2.21 nm water film is 6.61% higher than that without water film. The main reason was that when the thickness of the water film was 2.21 nm, the water film ruptured during the CO_2 oil recovery process. Due to the imbibition of water, the oil recovery in the dead-end pores became higher. When the thickness of the water film was 3.22 nm,

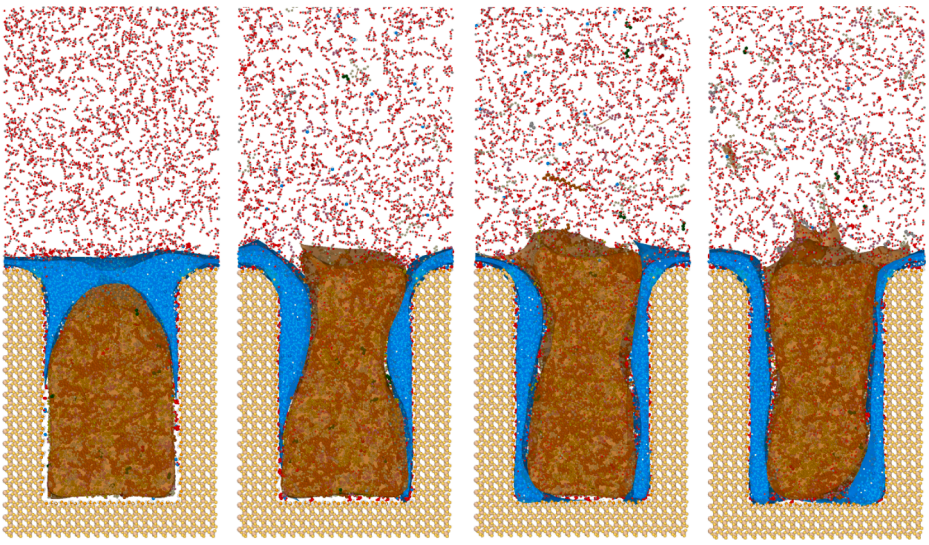

Fig. 25. Snapshots of water film thickness of 2.21 nm at different times.

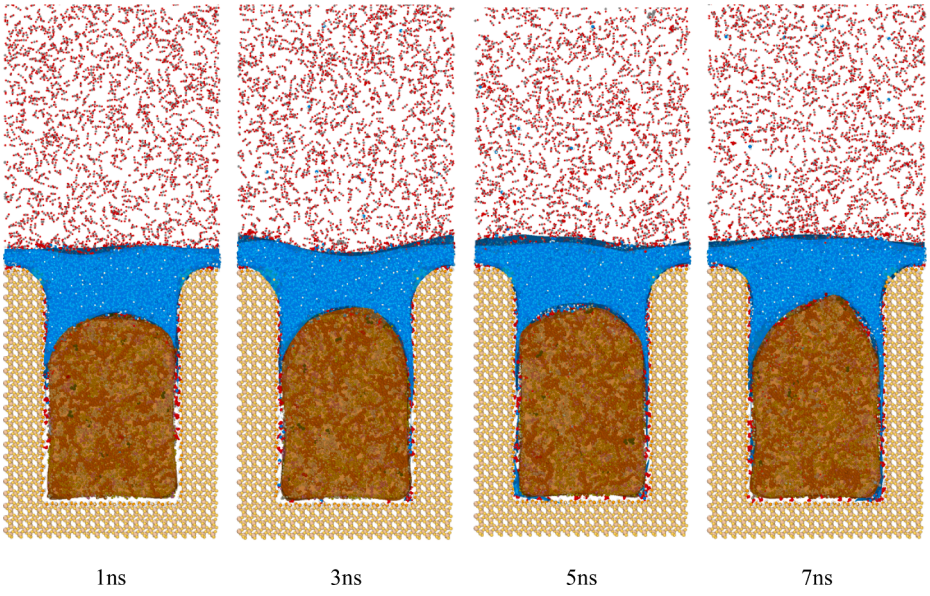

Fig. 26. Snapshots of water film thickness of 3.22 nm at different times.

the water film did not break through during the CO_2 flooding process, and the oil in the pores was difficult to recover. Due to the sealing effect of the water film, the recovery was 0%.

Fig. 29 shows the recovery of the different components in the oil with and without water membranes. With a water membrane, the light components of C1–C4 were recovered to a lower degree than the non-aqueous membrane. The recovery of C1–C4 was 65.46% with no water film, while the recovery of C1–C4 was 60.98% when the water film thickness was 2.21 nm. This was 4.48% lower than without a water membrane. The main reason was that with a water membrane, the oil could not make direct contact with the CO_2, and the light components in the oil were not extracted into the CO_2 at the beginning, which caused the recovery of the C1–C4 degree to decrease. However, in the dead-end pores with a water film thickness of 2.21 nm, the recovery of other components was higher than without the water film. The main reason was that the ability of CO_2 to extract heavy components was weakened. After the water film breakthrough, the heavy components were extracted due to the imbibition of water. The recovery of C30 was 0.0% with no water film, while the recovery of C30 was 5.67% when the water film thickness was 2.21 nm. In the presence of water film, it was more beneficial for the recovery of heavy components in oil; however, if the water film could not be broken through, it would have no effect on the recovery of all components in the pores.

5. Conclusion

In this paper, MD simulations were applied to study the microcosmic recovery mechanism of multi-oil components in nanopores from the perspective of DPAA and the DFAA during the CO_2-EOR process.

In the nanopores, CO_2 can increase the oil potential energy, thereby making the oil more easily extracted from the nanopores. Meanwhile, the dissolution of CO_2 in the oil causes the oil to expand, and the closer to the CO_2-oil interface, the more pronounced the expansion of the oil. In the DPAA, the study on CO_2 injection rates found that the higher the CO_2 injection rate, the lower the displacement efficiency of oil. In addition, under the same injection rate, it takes less time a 6 nm single pore than a 6 nm pore of double pores to achieve the same displacement efficiency. The oil recovery of no water film and different water film thicknesses are

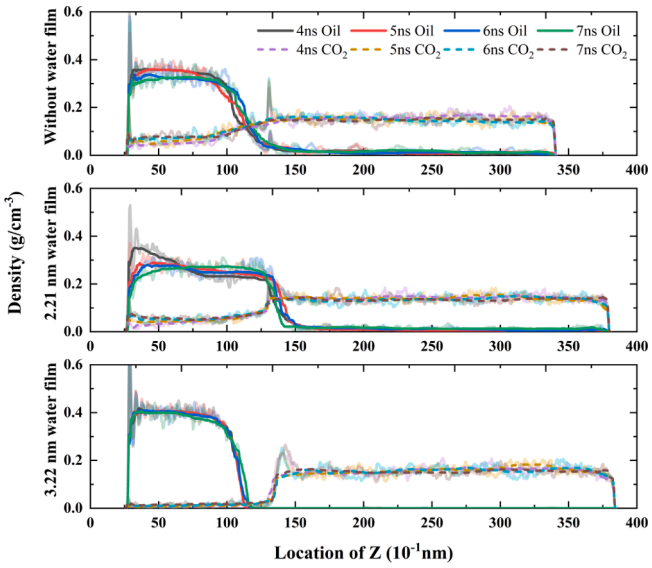

Fig. 27. Density distribution of CO_2 and oil under different water film thickness.

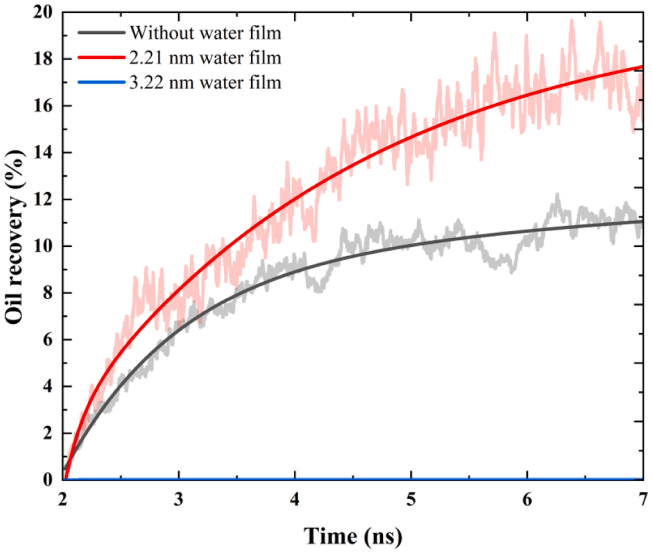

Fig. 28. Oil recovery factor under different water film thickness.

analyzed in the DFAA. It is found that the existence of water film helps recover oil molecules of heavy components, but whether the water film can break through after CO_2 injection is the key to oil recovery from dead pores. If the water film can be broken through, the existence of the water film will help the production of oil in the dead pores. On the contrary, the presence of the water film is a blockade effect on the oil in the dead pores, and it is difficult for CO_2 to recover the oil in the dead pores. Therefore, it has particular reference significance for CO_2 EOR and CO_2 storage in oilfields with high water content.

CRediT authorship contribution statement

Yongcheng Luo: Conceptualization, Writing – original draft, Investigation, Methodology, Data curation, Formal analysis, Visualization. **Xiangui Liu:** Project administration. **Hanmin Xiao:** Resources, Funding acquisition, Supervision. **Taiyi Zheng:** Writing – review & editing, Validation, Investigation.

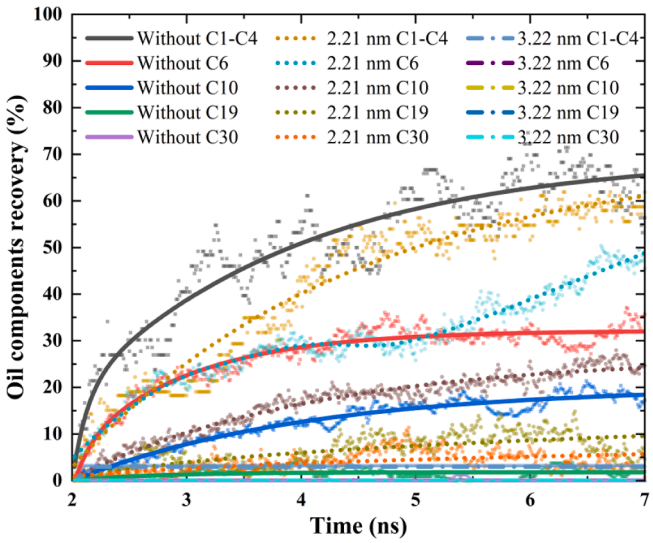

Fig. 29. Recovery factor of oil components under different water film thickness.

Declaration of Competing Interest

The authors declare that they have no known competing financial interests or personal relationships that could have appeared to influence the work reported in this paper.

Data availability

No data was used for the research described in the article.

Acknowledgements

This work was supported by the China National Petroleum Corporation (CNPC) basic advanced reserve technology (2021DJ2201).

Appendix A. Supplementary material

Supplementary data to this article can be found online at https://doi.org/10.1016/j.seppur.2022.122607.

References

[1] S. Xua, K. Z, Y. Yan. Molecular insight into disassociation mechanism of tight oil in core–shell nanofluids flooding. Chemical Physics Letters 804 (2022), 139849. 10.1016/j.cplett.2022.139849.
[2] Q. Zhou, D. Zhang, X. Li, Z. Qian, G. Chen, C. Lyu, X. Ma, C. Li, Insight into the desorption behavior and mechanism of tight oil with in-situ low-temperature thermal, J. Petrol. Sci. Eng. 218 (2022), 111001, https://doi.org/10.1016/j.petrol.2022.111001.
[3] S. Xu, J. Guo, Q. Feng, G. Ren, Y. Li, S. Wang, Optimization of hydraulic fracturing treatment parameters to maximize economic benefit in tight oil, Fuel 329 (2022), 125329, https://doi.org/10.1016/j.fuel.2022.125329.
[4] Administration EI. Energy information administration. 2020, Available from: https://www.eia.gov/.
[5] Y. Yang, W. Xiao, Y. Bernabe, Q. Xie, J. Wang, Y. He, M. Li, M. Chen, J. Ren, J. Zhao, L. Zheng, Effect of pore structure and injection pressure on waterflooding in tight oil sandstone cores using NMR technique and pore network simulation, J. Petrol. Sci. Eng. 217 (2022), 110886, https://doi.org/10.1016/j.petrol.2022.110886.
[6] M. Chen, J. Dai, X. Liu, Y. Kuang, Z. Wang, S. Gou, M. Qin, M. Li, Effect of displacement rates on fluid distributions and dynamics during water flooding in tight oil sandstone cores from nuclear magnetic resonance (NMR), J. Petrol. Sci. Eng. 184 (2020), 106588, https://doi.org/10.1016/j.petrol.2019.106588.
[7] G. Qin, X. Dai, L. Sui, M. Geng, L. Sun, Y. Zheng, Y. Bai, Study of massive water huff-n-puff technique in tight oil field and its field application, J. Petrol. Sci. Eng. 196 (2021), 107514, https://doi.org/10.1016/j.petrol.2020.107514.
[8] Z. Song, Y. Song, Y. Li, B. Bai, K. Song, J. Hou, A critical review of CO_2 enhanced oil recovery in tight oil reservoirs of North America and China, Fuel 276 (2020), 118006, https://doi.org/10.1016/j.fuel.2020.118006.

[9] D. Ren, X. Wang, Z. Kou, S. Wang, H. Wang, X. Wang, Y. Tang, Z. Jiao, D. Zhou, R. Zhang, Feasibility evaluation of CO EOR and storage in tight oil reservoirs: A demonstration project in the Ordos Basin, Fuel 331 (2023), 125652, https://doi.org/10.1016/j.fuel.2022.125652.

[10] J. Liu, H. Li, Q. Tan, S. Liu, H. Zhao, Z. Wang, Quantitative study of CO_2 huff-n-puff enhanced oil recovery in tight formation using online NMR technology, J. Petrol. Sci. Eng. 216 (2022), 110688, https://doi.org/10.1016/j.petrol.2022.110688.

[11] L. Wang, Y. He, Q. Wang, M. Liu, X. Jin, Multiphase flow characteristics and EOR mechanism of immiscible CO_2 water-alternating-gas injection after continuous CO_2 injection: A micro-scale visual investigation, Fuel 282 (2020), 118689, https://doi.org/10.1016/j.fuel.2020.118689.

[12] A.H. Fath, A.R. Pouranfard, Evaluation of miscible and immiscible CO_2 injection in one of the Iranian oil fields, Egypt. J. Pet. 23 (2014) 255–270, https://doi.org/10.1016/j.ejpe.2014.08.002.

[13] S.M. Seyyedsar, M. Sohrabi, Visualization observation of formation of a new oil phase during immiscible dense CO_2 injection in porous media, J. Mol. Liq. 241 (2017) 199–210, https://doi.org/10.1016/j.molliq.2017.05.146.

[14] Z. Li, Y. Su, L. Li, Y. Hao, W. Wang, Y. Meng, A. Zhao, Evaluation of CO_2 storage of water alternating gas flooding using experimental and numerical simulation methods, Fuel 311 (2022), 122489, https://doi.org/10.1016/j.fuel.2021.122489.

[15] J. Snippe, S. Berg, K. Ganga, N. Brussee, R. Gdanski. Experimental and numerical investigation of wormholing during CO_2 storage and water alternating gas injection International Journal of Greenhouse Gas Control 94(2020) 102901. 10.1016/j.ijggc.2019.102901.

[16] W. Tang, J. Sheng, T. Jiang, Further discussion of CO_2 huff-n-puff mechanisms in tight oil reservoirs based on NMR monitored fluids spatial distributions, Pet. Sci. 23 (2022), https://doi.org/10.1016/j.petsci.2022.08.014.

[17] X. Wang, P. Xiao, Z. Yang, X. Liu, Z. Xia, L. Wang, Laboratory and field-scale parameter optimization of CO_2 huff–n–puff with the staged-fracturing horizontal well in tight oil reservoirs, J. Petrol. Sci. Eng. 186 (2020), 106703, https://doi.org/10.1016/j.petrol.2019.106703.

[18] W. Pu, D. Du, S. Wang, L. Zeng, R. Feng, S. Memon, J. Sarout, M.A. Varfolomeev, M. Sarmadivaleh, Q. Xie, Experimental study of CO_2 huff-n-puff in a tight conglomerate reservoir using true triaxial stress cell core fracturing and displacement system: A case study, J. Petrol. Sci. Eng. 199 (2021), 108298, https://doi.org/10.1016/j.petrol.2020.108298.

[19] M. Ding, Y. Wang, D. Liu, X. Wang, H. Zhao, W. Chen, Enhancing tight oil recovery using CO_2 huff and puff injection: An experimental study of the influencing factors, J. Nat. Gas Sci. Eng. 90 (2021), 103931, https://doi.org/10.1016/j.jngse.2021.103931.

[20] S. Afari, K. Ling, B. Sennaoui, D. Maxey, T. Oguntade, J. Porlles, Optimization of CO_2 huff-n-puff EOR in the Bakken Formation using numerical simulation and response surface methodology, J. Petrol. Sci. Eng. 215 (2022), 110552, https://doi.org/10.1016/j.petrol.2022.110552.

[21] X. Tang, Y. Li, X. Han, Y. Zhou, J. Zhan, M. Xu, R. Zhou, K. Cui, X. Chen, L. Wang, Dynamic characteristics and influencing factors of CO_2 huff and puff in tight oil reservoirs, Pet. Explor. Dev. 48 (2021) 946–955, https://doi.org/10.1016/S1876-3804(21)60079-4.

[22] Y. Luo, T. Zheng, H. Xiao, X. Liu, H. Zhan, Z. Wu, X. Zhao, D. Xia, Identification of distinctions of immiscible CO_2 huff and puff performance in Chang-7 tight sandstone oil reservoir by applying NMR, microscope and reservoir simulation, J. Petrol. Sci. Eng. 209 (2022), 109719, https://doi.org/10.1016/j.petrol.2021.109719.

[23] S. Wang, X. Yao, Q. Feng, F. Javadpour, Y. Yang, Q. Xue, X. Li, Molecular insights into carbon dioxide enhanced multi-component shale gas recovery and its sequestration in realistic kerogen, Chem. Eng. J. 425 (2021), 130292, https://doi.org/10.1016/j.cej.2021.130292.

[24] Y. Chang, S. Xiao, Y. Fu, X. Wang, Z. Zhang, J. He, Nanomechanical characteristics of trapped oil droplets with nanoparticles: A molecular dynamics simulation, J. Petrol. Sci. Eng. 203 (2021), 108649, https://doi.org/10.1016/j.petrol.2021.108649.

[25] H. Long, H. Lin, M. Yan, Y. Bai, X. Tong, X. Kong, S. Li, Adsorption and diffusion characteristics of CH4, CO_2, and N2 in micropores and mesopores of bituminous coal: Molecular dynamics, Fuel 292 (2021), 120268, https://doi.org/10.1016/j.fuel.2021.120268.

[26] S. Wang, F. Javadpour, Q. Feng, Molecular dynamics simulations of oil transport through inorganic nanopores in shale, Fuel 171 (2016) 74–86, https://doi.org/10.1016/j.fuel.2015.12.071.

[27] Y. Zhang, T. Fang, B. Ding, W. Wang, Y. Yan, Z. Li, W. Guo, J. Zhang, Migration of oil/methane mixture in shale inorganic nano-pore throat: A molecular dynamics simulation study, J. Petrol. Sci. Eng. 187 (2020), 106784, https://doi.org/10.1016/j.petrol.2019.106784.

[28] S. Wang, Y. Liang, Q. Feng, F. Javadpour, Sticky layers affect oil transport through the nanopores of realistic shale kerogen, Fuel 310 (2022), 122480, https://doi.org/10.1016/j.fuel.2021.122480.

[29] M. Sedghi, M. Piri, L. Goual, Molecular dynamics of wetting layer formation and forced water invasion in angular nanopores with mixed wettability, J. Chem. Phys. 141 (2014), 194703.

[30] B. Liu, C. Wang, J. Zhang, S. Xiao, Z. Zhang, Y. Shen, B. Sun, J. He, Displacement Mechanism of Oil in Shale Inorganic Nanopores by Supercritical Carbon Dioxide from Molecular Dynamics Simulations, Energy Fuels 31 (2017) 738–746, https://doi.org/10.1021/acs.energyfuels.6b02377.

[31] T. Fang, M. Wang, Y. Gao, Y. Zhang, Y. Yan, J. Zhang, Enhanced oil recovery with CO_2/N2 slug in low permeability reservoir: Molecular dynamics simulation, Chem. Eng. Sci. 197 (2019) 204–211, https://doi.org/10.1016/j.ces.2018.12.016.

[32] T. Fang, Y. Zhang, Y. Yan, Z. Wang, J. Zhang, Molecular insight into the oil extraction and transport in CO 2 flooding with reservoir depressurization, Int. J. Heat Mass Transf. 148 (2020), 119051, https://doi.org/10.1016/j.ijheatmasstransfer.2019.119051.

[33] D.Y. Moh, H. Zhang, S. Wang, X. Yin, R. Qiao, Soaking in CO_2 huff-n-puff: A single-nanopore scale study, Fuel 308 (2022), 122026, https://doi.org/10.1016/j.fuel.2021.122026.

[34] T.A. Ho, A. Striolo, Water and Methane in Shale Rocks: Flow Pattern Effects on Fluid Transport and Pore Structure, AIChE J. 61 (2015) 2993–2999, https://doi.org/10.1002/aic.14869.

[35] H. Xiong, D. Devegowda, L. Huang, EOR solvent-oil interaction in clay-hosted pores: Insights from molecular dynamics simulations, Fuel 249 (2019) 233–251, https://doi.org/10.1016/j.fuel.2019.03.104.

[36] M. Cui, R. Wang, C. Lv, Z. Lun, S. Zhao, Y. Wang, Y. Tang, Research on microscopic oil displacement mechanism of CO_2 EOR in extra-high water cut reservoirs, J. Pet. Sci. Eng. 154 (2017) 315–321.

[37] Y. Luan, B. Liu, P. Hao, K. Zhan, J. Liu, Oil displacement by supercritical CO_2 in a water cut dead-end pore: Molecular dynamics simulation, J. Petrol. Sci. Eng. 188 (2020), 106899, https://doi.org/10.1016/j.petrol.2019.106899.

[38] Y. Luan, X. Dou, Y. Zhou, P. Hao, B. Liu, J. Liu, Effect of the water film rupture on the oil displacement by supercritical CO_2 in the nanopore: molecular dynamics simulations, Energy Fuels 36 (2022) 4348–4357, https://doi.org/10.1021/acs.energyfuels.2c00414.

[39] C. Li, H. Pu, X. Zhong, Y. Li, J.X. Zhao, Interfacial interactions between Bakken crude oil and injected gases at reservoir temperature: A molecular dynamics simulation study, Fuel 276 (2020), 118058, https://doi.org/10.1016/j.fuel.2020.118058.

[40] F. Peng, R. Wang, Z. Guo, G. Feng, Molecular dynamics simulation to estimate minimum miscibility pressure for oil with pure and impure CO_2, J Phys Commun 2 (2018), 115028, https://doi.org/10.1088/2399-6528/aaf090.

[41] P.C. Myint, A. Firoozabadi, Thin liquid films in improved oil recovery from lowsalinity brine, Curr Opin Colloid Interface Sci 20 (2015) 105–114.

[42] Y. Yan, Z. Dong, Y. Zhang, P. Wang, T. Fang, J. Zhang, CO_2 activating hydrocarbon transport across nanopore throat: insights from molecular dynamics simulation, Phys. Chem. Chem. Phys. 19 (2017) 30439, https://doi.org/10.1039/c7cp05759h.

[43] C.M. Koretsky, D.A. Sverjensky, N. Sahai, A model of surface site types on oxide and silicate minerals based on crystal chemistry: implications for site types and densities, multi-site adsorption, surface infrared spectroscopy, and dissolution kinetics, Am. J. Sci. 298 (1998) 349–438.

[44] J.G. Harris, K.H. Yung, Carbon Dioxide's Liquid-Vapor Coexistence Curve and Critical Properties As Predicted by a Simple Molecular Model, J. Phys. Chem. 99 (1995) 12021–12024, https://doi.org/10.1021/j100031a034.

[45] M.G. Martin, J.I. Siepmann, Transferable potentials for phase equilibria. 1. unitedatom description of n-alkanes. J Phys Chem B 102(1998), 2569–77, 10.1021/jp990822m.

[46] S.K. Nath, F.A. Escobedo, J.J. De Pablo, On the simulation of vapor-liquid equilibria for alkanes, J Chem Phys 108 (1998) 9905–9911, https://doi.org/10.1063/1.476429.

[47] P. Mark, L. Nilsson, Structure and Dynamics of the TIP3P, SPC, and SPC/E Water Models at 298 K, J. Phys. Chem. A 105 (2001) 9954–9960, https://doi.org/10.1021/jp003020w.

[48] R.T. Cygan, J.J. Liang, A.G. Kalinichev, Molecular models of hydroxide, oxyhydroxide, and clay phases and the development of a general force field, J. Phys. Chem. B 108 (2004) 1255–1266.

[49] M. Szczerba, D.K. McCarty, A. Derkowski, M. Kowalik, Molecular dynamics simulations of interactions of organic molecules found in oil with smectite: Influence of brine chemistry on oil recovery, J. Petrol. Sci. Eng. 191 (2020), 107148, https://doi.org/10.1016/j.petrol.2020.107148.

[50] Y. Zhang, W. Guo, Molecular insight into the tight oil movability in nano-pore throat systems, Fuel 293 (2021), 120428, https://doi.org/10.1016/j.fuel.2021.120428.

[51] G. Xu, H. Wang, Molecular dynamics study of oxidative aging effect on asphalt binder properties, Fuel 188 (2017) 1–10, https://doi.org/10.1016/j.fuel.2016.10.021.

[52] B. Liu, J. Shi, M. Wang, J. Zhang, B. Sunb, Y. Shen, X. Sun, Reduction in interfacial tension of water–oil interface by supercritical CO_2 in enhanced oil recovery processes studied with molecular dynamics simulation, J. of Supercritical Fluids 111 (2016) 171–178, https://doi.org/10.1016/j.supflu.2015.11.001.

[53] H.J.C. Berendsen, J.P.M. Postma, W.F. Gunsteren, A. DiNola, J.R. Haak, Molecular dynamics with coupling to an external bath, J. Chem. Phys. 81 (1984) 3684–3690.

[54] A. Baban, A.A. Yaseri, A. Keshavarz, R. Amin, S. Iglauer, CO_2 – brine – sandstone wettability evaluation at reservoir conditions via Nuclear Magnetic Resonance measurements, Int. J. Greenhouse Gas Control 111 (2021), 103435, https://doi.org/10.1016/j.ijggc.2021.103435.

[55] A. Baban, A. Keshavarz, R. Amin, S. Iglauer, Residual Trapping of CO_2 and Enhanced Oil Recovery in Oil-Wet Sandstone Core – A Three-Phase Pore-Scale Analysis Using NMR, Fuel 332 (2023), 126000, https://doi.org/10.1016/j.fuel.2022.126000.

[56] G. Cao, Y. Bai, X. Nan, H. An, L. Wang, T. Du, D. Li, Effect of supercritical carbon dioxide adsorption on oil displacement in tight reservoir, Case Stud. Therm. Eng. 24 (2021), 100880, https://doi.org/10.1016/j.csite.2021.100880.

[57] X. Wang, Z. Zhang, J. Zhang, J. He, Insight into the pressure-induced displacement mechanism for selecting efficient nanofluids in various capillaries, Environ. Sci. Nano 7 (2020) 2785, https://doi.org/10.1039/d0en00462f.
[58] B. Cao, X. Lu, K. Xie, H. Ding, Z. Xiao, W. Cao, Y. Zhou, X. He, Y. Li, H. Li, The pore-scale mechanisms of surfactant-assisted spontaneous and forced imbibition in water-wet tight oil reservoirs, J. Petrol. Sci. Eng. 213 (2022), 110371, https://doi.org/10.1016/j.petrol.2022.110371.
[59] S. Li, S. Yang, X. Gao, M. Wang, J. iYu. Experimental study on liquid production law, oil recovery mechanism, and influencing factors of water huff-n-puff in the tight sedimentary tuff oil reservoir, J. Petrol. Sci. Eng. 208 (2022) 109721. 10.1016/j.petrol.2021.109721.